Carbonation of mantle peridotites at the Atlantis Massif: Insights from IODP Expedition 357

Lotta Ternieten[1], Gretchen L Früh-Green[1] and Stefano M Bernasconi[1]

[1]Department of Earth Science, ETH Zurich, Clausiusstrasse 25, 8092, Zurich, Switzerland.

Corresponding author: Lotta Ternieten (lotta.ternieten@erdw.ethz.ch)

Key Points:

- A conceptual model places carbonate formation in a time frame with mafic intrusions and fluid heterogeneities during hydration of the AM
- CO_2 capture is limited in the shallower crust, concentrated around the active LCHF, but may be more extended in deeper circulation
- Magnesite and dolomite formed at high Mg/Ca ratios and zones of channelled flow in serpentinized peridotites at the Atlantis Massif

Abstract

Petrographic and major element investigations on carbonates from drill cores recovered during IODP Expedition 357 on the Atlantis Massif (AM) provide information on the genesis of carbonate minerals in the oceanic lithosphere. Textural sequences and mineralogical assemblages reveal three distinct types of carbonate occurrences in ultramafic rocks that are controlled by (i) fluid composition and flow, (ii) temperature of the system, and (iii) the presence of mafic intrusions. The first occurrence of carbonate consists of different generations of calcite that formed syn- to post- serpentinization. These calcites formed at temperatures between 30 and 185°C (based on clumped isotopes) and from a fluid influenced by interaction with mafic intrusions. The second occurrence consists of magnesite, dolomite, calcite and aragonite veins that also formed syn- to post serpentinization. These carbonates formed at temperatures between 4 and 188°C and from fluids with highly variable composition and Mg/Ca ratios, but overall high CO_2 and moderate SiO_2 concentrations. High FeO (3.3 wt%) and MnO (7.3 wt%) contents indicate high temperatures, high water/rock ratios, and low oxygen fugacity for both carbonate assemblages. The third occurrence consists solely of aragonite veins formed at low-temperatures (5°C) within the uplifted serpentinized peridotites. Chemical data suggest that aragonite precipitated from cold seawater, which underwent little exchange with the basement. Combining these observations, we propose a model that places different carbonate occurrences in a conceptual frame involving mafic intrusions in the peridotites and fluid heterogeneities during progressive exhumation and alteration of the AM.

1 Introduction

Mantle peridotites undergo hydrothermal alteration when exposed to aqueous fluids at mid-ocean ridges (MORs), continental margins, subduction zone fore-arcs, and ophiolites, which has significant consequences for the thermal structure and rheology of the oceanic lithosphere, geochemical budgets of the ocean, and microbial processes within and at the seafloor (e.g., Früh-Green et al., 2004; Kelley & Früh-Green, 2001; Lister, 1972; Proskurowski et al., 2006; Wheat & Mottl, 2004). Seawater circulation through the ocean crust occurs at rates such that circulation of the entire volume of the ocean through the oceanic crust requires less than 20 Myr (German & Von Damm, 2003; Wheat & Mottl, 2004). The resulting hydrothermal alteration of peridotites leads to the formation of hydrous silicates, oxides, sulfides and carbonates (e.g., Frost, 1985).

The mechanisms that drive carbonate precipitation have been a subject of study for many years (Frost, 1985; Greenwood, J., 1967; Hansen et al., 2005; Hess, 1933; Koons, 1981; Korzhinskii, 1959; Schandl & Naldrett, 1992; Trommsdorff & Evans, 1977). Carbonates can precipitate over a wide range of pressure and temperature conditions and in various settings. In shallow parts of the oceanic lithosphere, carbonates can form during conductive heating of seawater, conductive cooling of hydrothermal fluids, mixing of hydrothermal fluids with seawater, and metasomatic replacement reactions (e.g., Alt et al., 2013; Bach et al., 2011; Grozeva et al., 2017; Klein et al., 2015; Schroeder et al., 2015; Schwarzenbach, Früh-Green, et al., 2013). More recently, carbonate formation has received considerable attention as a means to sequester atmospheric CO_2 and reduce global warming (Kelemen et al., 2011; Seifritz, 1990). Previous studies indicate that 5 – 9% of the rocks exposed along slow- and ultraslow-spreading MORs consist of hydrothermally altered peridotite (Cannat et al., 2010; Carlson, 2001) that can host carbonates. This makes carbonate formation in ultramafic rocks a potentially significant sink for carbon in the shallow oceanic lithosphere, but one that remains poorly quantified.

Several field, experimental and theoretical studies have been conducted with the main focus on the carbonation of olivine to magnesite (Andreani et al., 2009; Bruni et al., 2002; Cipolli et al., 2004; Giammar et al., 2005; Hansen et al., 2005; Hövelmann et al., 2011; Kelemen & Matter, 2008; King et al., 2010; Klein & Garrido, 2011; Klein & McCollom, 2013; Lafay et al., 2014; Van Noort et al., 2013; Paukert et al., 2012; Peuble, Andreani, et al., 2015). Magnesite formation is a widespread alteration reaction of hydrothermally altered peridotites on land and can be found

mainly within ophiolites in orogenic belts and exhumed mélange rocks in paleo-subduction zones (Barnes et al., 1973; Beinlich et al., 2012; Bohlke, 1989; Boschi et al., 2009; Dabitzias, 1980; Falk & Kelemen, 2015; Hansen et al., 2005; Naldrett, 1966; Robinson et al., 2005; Schandl & Wicks, 1991; Spandler et al., 2008; Ulrich et al., 2014), or within highly serpentinized peridotites that have been affected by low-temperature alteration by Mg- and HCO_3-rich meteoric waters (Barnes & O'Neil, 1969; Bruni et al., 2002; Kelemen et al., 2011; Kelemen & Matter, 2008; Paukert et al., 2012; Schwarzenbach et al., 2016). However, magnesite precipitation in oceanic peridotites has only been described in a few studies (Gablina et al., 2006). Instead, aragonite, calcite and less commonly dolomite are reported from hydrated mafic and ultramafic rocks in oceanic settings (Bach et al., 2011; Bonatti et al., 1974; Eickmann, Bach, Rosner, et al., 2009; Kelemen et al., 2011; Ludwig et al., 2006; Schroeder et al., 2015; Schwarzenbach, Lang, et al., 2013). Hydration and alteration experiments with ultramafic rocks show that dolomite or magnesite do not precipitate even in supersaturated systems in which dolomite and magnesite formation is thermodynamically predicted (Grozeva et al., 2017; Hövelmann et al., 2011). Grozeva et al. (2017) assumed that the Mg/Ca ratio of the reacting fluid at the mineral scale ultimately controls whether magnesite, dolomite, or calcite forms in seafloor serpentinization systems. In contrast, Hövelmann et al. (2011) suggest that kinetic factors impede the formation of Mg-bearing carbonates relative to Ca-carbonates. It is known that during hydrothermal alteration of mantle peridotites, differences in fluid flow significantly change the local solution chemistry, which in turn affect carbonate formation. However, it remains unclear what factors directly control carbonate mineralogy in a natural system and what role fluid-rock interactions play during carbonate precipitation.

Here we present a study of serpentinized peridotites and metabasic rocks from the Atlantis Massif (AM) close to the Lost City Hydrothermal Field (LCHF) that were recovered during International Ocean Discovery Program (IODP) Expedition 357 (Früh-Green et al., 2017). The Lost City Hydrothermal Field located on the southern wall of the Atlantis Massif is considered an end-member for serpentinite-hosted, hydrothermally active systems at the slow-spreading Mid-Atlantic Ridge (MAR). It is an off-axis, low-temperature, peridotite-dominated submarine venting environment driven by seawater migration along deeply penetrating fault systems that facilitate hydration of the plutonic crust and serpentinization of the upper mantle (Kelley et al., 2001, 2005). Similar to other hydrothermal systems, the LCHF is characterized by fluids that are strongly enriched in Ca and depleted in Mg (e.g., Seyfried et al., 2015), whereby Ca is believed to be derived

from dissolution of pyroxene (Douville et al., 2002; Gamo et al., 2001; Kelley et al., 2005) or related to silica metasomatism of surrounding mafic domains (Berndt et al., 1989; Bischoff & Dickson, 1975). However, unlike fluids venting from unsedimented, basalt-hosted hydrothermal systems that are typically enriched in CO_2 (Von Damm et al., 1998; Lilley et al., 2003), the LCHF fluids are highly alkaline and depleted in CO_2, suggesting that they have lost oxidized carbon at depth, either due to metasomatic replacement of minerals or precipitation of carbonates (Proskurowski et al., 2008).

In this study, we investigated the carbonate population at the Atlantis Massif to constrain the composition and physico-chemical properties of the precipitating fluid (e.g., Bonatti et al., 1980; Eickmann, Bach, Rosner, et al., 2009; Früh-Green et al., 2003) and to better understand the hydrothermal evolution of the Atlantis Massif. We performed detailed analyses of the chemical and petrological characteristics of the carbonates within the basement, which highlight the complexity of this unique system and allow us to examine the crucial roles that protolith and fluid composition play in regulating carbonate formation during interaction of hydrothermal fluids and peridotite.

2 Geological setting and sampling

The Atlantis Massif, located at 30°N along the slow-spreading Mid-Atlantic Ridge (MAR), is a 1.5-2 Myr old, dome-like massif forming the inside corner of the intersection between the MAR and the Atlantis Transform Fault (ATF) (Figure 1). The massif is interpreted as an oceanic core complex (OCC), comprised of lower crustal and upper mantle rocks that were uplifted and exposed by long-lived, low-angle detachment faulting (Blackman et al., 1998, 2002; Cann et al., 1997; Karson et al., 2006). Three lithologic domains can be distinguished: the corrugated central dome comprising mafic rocks ranging from olivine-rich troctolites to oxide gabbros; the variably altered peridotite-dominated southern wall with intermittent mafic plutonic intrusions, which is part of the Southern Ridge and defines the edge of the ATF; and the eastern basaltic block, which is interpreted as the hanging wall of the OCC. The summit peak rises to depths of less than 750 m and is located about midway along the length of the Southern Ridge. The top of the massif is covered by pelagic sediments, rubble, and sedimentary breccias (Blackman et al., 2002; Boschi et al., 2006; Früh-Green et al., 2003; Karson et al., 2006; Schroeder et al., 2002).

The Lost City Hydrothermal Field is located on a fault-bounded terrace just below the top of the southern wall near the summit. It is composed of numerous active and inactive, up to 60 m tall, carbonate-brucite chimneys that vent low-temperature (40 - 95°C), alkaline (pH 9 - 11) fluids (Kelley et al., 2001, 2005; Ludwig et al., 2006; Seyfried et al., 2015). The vent fluids are characterized by low silica, metal and CO_2 concentrations and high CH_4 (1 - 2 mmol/kg), H_2 (up to 15 mmol/kg), Ca (~30 mmol/kg), and low-molecular-weight hydrocarbons concentrations. Hydrothermal circulation is believed to be driven by residual crustal heat and lithosphere cooling, with the composition of the fluids controlled by subsurface serpentinization reactions in the underlying mantle rocks. The hydrothermal activity has been on-going for at least 30,000 years (Früh-Green et al., 2003; Kelley et al., 2001, 2005) and subsequent U - Th analyses indicated that this is a minimum age as some of the carbonate deposits yielded ages of up to 120,000 years (Ludwig et al., 2011).

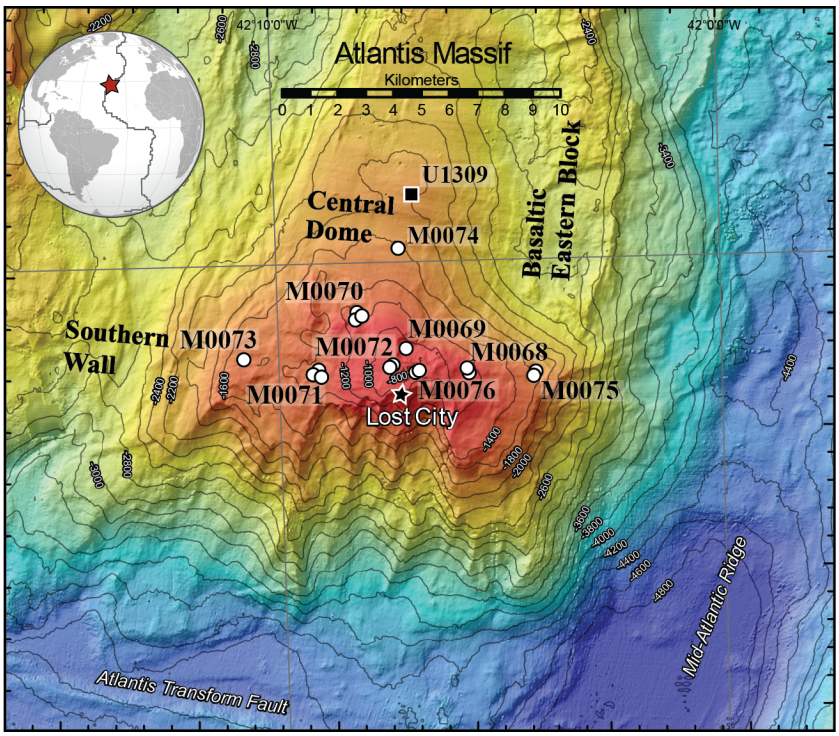

Figure 1. Map of the Atlantis Massif, located at the inside corner of the intersection between the Mid-Atlantic Ridge and the Atlantis Transform Fault, showing the locations of the study sites (M0068, M0069, M0070, M0071, M0072, M0073, M0074, M0075, M0076) drilled during IODP Expedition 357 (Früh-Green at al., 2017). The black square indicates IODP Site U1309 (IODP

Expeditions 304 and 305, Blackman et al., 2006). The black star indicates the location of the Lost City Hydrothermal Field (Kelley et al., 2001).

2.1 IODP Expedition 357

IODP Expedition 357 drilled seventeen shallow boreholes (from 1.3 mbsf to maximum 16.4 mbsf) at nine sites along an east-west trending transect across the Atlantis Massif (Figure 1). Two sites are on the eastern end of the southern wall (Sites M0068 and M0075), three along the centre of the southern wall north of the LCHF (Sites M0069, M0072, and M0076), two on the western end (Sites M0071 and M0073), and two north of the southern wall (Sites M0070 and M0074) in the direction of the central dome of the massif and Integrated Ocean Drilling Program Site U1309. Overall, the recovered ultramafic rocks reveal a high and heterogeneous degree of serpentinization, as well as metasomatic talc-amphibole-chlorite overprinting and local rodingitization (Früh-Green et al., 2017, 2018). Contacts between ultramafic rocks and gabbroic domains are marked by silica metasomatism with the appearance of talc, tremolite and chlorite (central IODP Holes M0068B, M0072B and M0076B) in part replacing pyroxenes, which indicates that hydration at some sites may have started at temperatures in the range of 400 - 500°C and that pyroxene alteration pre-dates the onset of serpentinization (Rouméjon, Früh-Green, et al., 2018; Schroeder & John, 2004). Field and geophysical studies estimated that at least ~20 % of the massif is completely serpentinized (Detrick & Collins, 1998; Früh-Green et al., 2003; Nooner et al., 2003), whereby two main stages dominate serpentinization. All harzburgites and dunites have undergone an initial stage of pervasive serpentinization, at 200 - 350°C (Boschi et al., 2008; Rouméjon, Früh-Green, et al., 2018; Rouméjon, Williams, et al., 2018). The second stage of serpentinization is dominated by localized fluid pathways and more focused and intense fluid-rock interaction leading to recrystallization and vein formation dominated by chrysotile or antigorite (Rouméjon, Früh-Green, et al., 2018).

This study focuses mainly on the five sites containing altered peridotite (Sites M0071, M0072, M0069, M0076 and M0068, Figure 2). The four remaining sites include foraminifera-bearing carbonate ooze, rubble blocks of variable lithologies and sedimentary breccia with volcanic clasts and carbonate sediments (Früh-Green et al., 2017). The sites considered here have a core recovery ranging between 30 % (Hole M0071C) and 75 % (Hole M0069A), with an average

176 recovery of 58 %. Drill cores of IODP Expedition 357 are described in detail in Früh-Green et al.
177 (2017, 2018, supplementary material), and Rouméjon, Früh-Green, et al. (2018, supplementary
178 material).

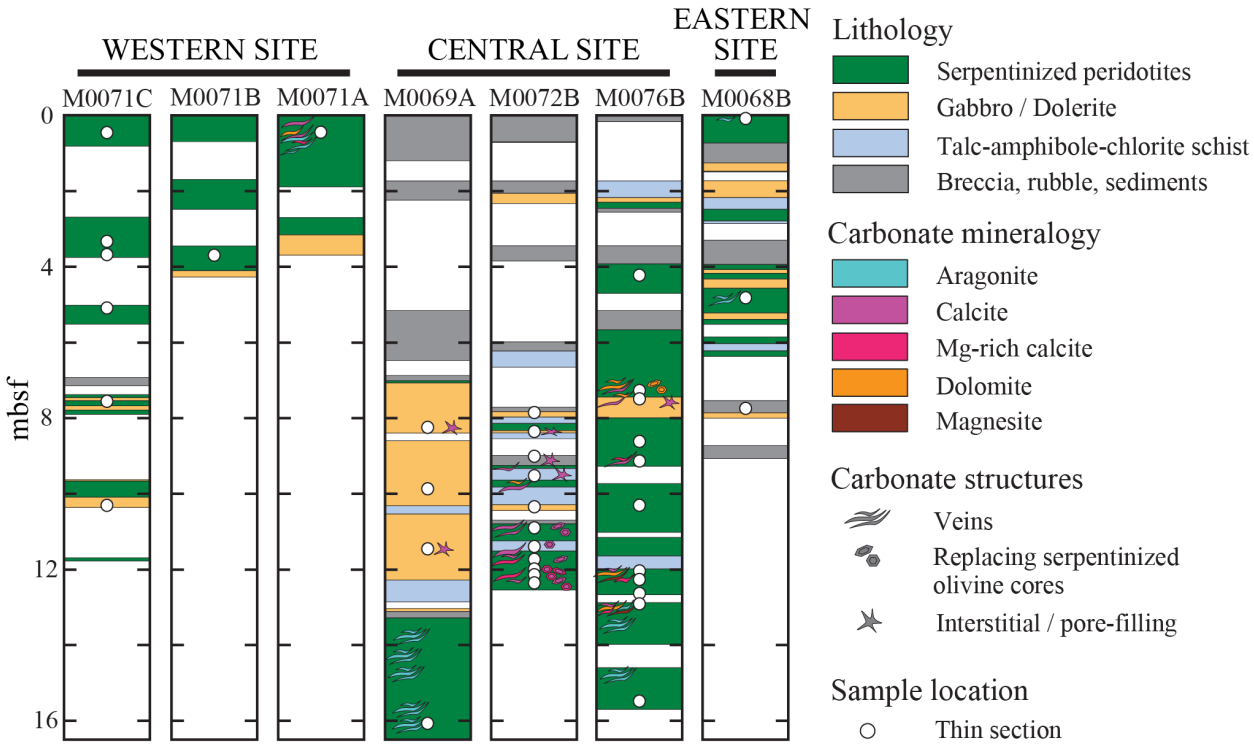

179

180 **Figure 2.** Simplified downhole logs of the dominant lithologies recovered in the seven holes
181 containing serpentinized peridotites. The western and eastern sites exhibit rubbly intervals and
182 sedimentary structures pointing to a mass-wasting origin and local faulting. The central sites
183 represent in-situ portions of the detachment footwall (Früh-Green et al., 2017; Rouméjon et al.,
184 2018a). Serpentinized peridotites from Hole M0071A, M0069A and M0068B are dominated by
185 aragonite veins. In contrast, serpentinites from Hole M0072B have dominantly calcite and Mg-
186 rich calcite occurring in veins and serpentinized olivine cores, and one dolomite vein. Hole
187 M0076B is the only hole that exhibits aragonite, calcite, Mg-rich calcite, dolomite and magnesite

188 veins, as well as dolomite in serpentinized olivine cores. The 37 white dots indicate locations of
189 thin section samples.

190

191 **3 Analytical methods**

192 Petrographic investigations were made on 37 double-sided, polished thin sections of
193 representative samples distributed over five sites (7 holes), covering the diversity of rock types
194 and alteration textures. The sample-set consists of 24 peridotites (21 harzburgites and 3 dunites),
195 nine mafic rocks (4 gabbroic rocks, 5 doleritic rocks), two talc-amphibole ± chlorite schists and
196 two brecciated samples. Sample locations within the drill holes are indicated in Figure 2, together
197 with a simplified lithostratigraphy and location of identified carbonate occurrences. Samples are
198 named according to the IODP style guide: Expedition_Driling-Platform, Site, Hole_Core,
199 Coretype_Section_Interval in cm; (e.g., 357_M0076B_9R_1_5-9, Table 1). For simplicity, we
200 have removed the expedition and drilling platform information that remains the same for all
201 investigated samples (e.g., 76B_9R_1_5-9). We use clumped isotope data and radiocarbon ages
202 from a parallel study that investigates the identical set of carbonate veins (Ternieten et al., in prep.).

203 3.1 Powder X-ray diffraction

204 For mineralogical identification of carbonate veins, rock samples were cleaned with 2-
205 propanol and compressed air. In the first step, the surfaces of the veins were removed and
206 discarded, followed by sampling of the veins. The carbonate powder was homogenized by hand
207 using an agate mortar previously cleaned with dichloromethane (DCM). Crystallographic analyses
208 were made using a Bruker AXS D8 Advance Powder X-ray Diffractometer (XRD) equipped with
209 a Lynxeye superspeed detector (Bruker Corporation, Billerica, United States) with Cu Kα X-ray
210 radiation 2θ ranging between 10° to 60°, a voltage of 45 kV and a current of 40 mA, step size of
211 0.01°, and measurement time of 1 s per step. Quantification of the mineralogy of powdered
212 samples was carried out using the program PowDll (Kourkoumelis, 2013) and the RRUFF
213 database (Lafuente et al., 2015).

3.2 Optical and electron microscopy

Petrographic analyses were conducted using a polarizing microscope (Carl Zeiss Microscopy GmbH, Göttingen, Germany) on polished thin-sections. Characterization, distribution and textures of carbonates on polished thin-sections were conducted using a cold cathode cathodoluminescence (CL) CL8200 Mk5-2 (Cambridge Image Technology Ltd, Hertfordshire, UK) with a Nikon microscope (Nikon, Japan) interfaced with a Zeiss Axiocam camera (Carl Zeiss Microscopy GmbH, Göttingen, Germany). Operation conditions were set at an accelerating voltage of 15 kV with a beam current of 250 to 300 µA.

Major element composition of selected carbonates was determined using a five-spectrometer JEOL JXA-8200 and JEOL JXA-8230 Electron Probe Microanalyser (EPMA) (JEOL, Akishima, Japan) operating in wavelength-dispersion mode with an accelerating voltage of 15 kV and a current of 10 nA to 5 nA. EPMA analyses were carried out on polished and carbon-coated thin sections. Beam diameter was 10 µm, 5 µm and 2 µm, and count times varied from 20 to 60 s per element. The program Probe for EPMA (Probe Software Inc., Eugene, United States) was used along with the time-dependent intensity (TDI) correction to counteract the effect of beam damage when a drift in the intensity was observed. The mean atomic number background correction was used to correct for the background (Donovan et al., 2016; Donovan & Tingle, 1996). Elements analyzed are Si, Mg, Al, Ba, Ca, Fe, Mn and Sr calculated based on a set of natural and synthetic standards. For most elements with concentrations > 1 wt%, average precision is better than 1 %, and the average accuracy is better than 2 %. The data are quoted as oxide-weight per cent. Analyses of phases that yielded SiO_2 concentrations above 0.1 wt% have been excluded from our study, as they likely reflect mixed phases with surrounding serpentine or other silicate minerals. Because crystal size was commonly very small, it is difficult to obtain good analyses by electron microprobe, and twenty-three analyses of dolomite, replacing the cores of olivine crystals, with $SiO_2 < 4$ wt%, are included here.

Table 1. Carbonate occurrences and mineralogy in ultramafic and mafic rocks from the southern wall of the Atlantis Massif.

Sample	Site	Hole	Core	Section	Interval (cm) top	Interval (cm) bot.	Depth (mbsf) top	Depth (mbsf) bot.	Type of the rock	Carbonate occurrences	Carbonate mineralogy
71A-1R1-02	71	A	1	1	45	48	0.45	0.48	Serpentinized dunite	carb vein	arg, cc IIa, cc IIb, dol
71B-3R1-02	71	B	3	1	27	29	3.71	3.73	Serpentinized harzburgite	-	-
71C-1R1-01	71	C	1	1	46	50	0.46	0.50	Serpentinized harzburgite	-	-
71C-2R1-01	71	C	2	1	67	77	3.35	3.45	Serpentinized harzburgite	-	-
71C-2RCC-01	71	C	2	CC	5	9	3.70	3.74	Serpentinized harzburgite	-	-
71C-3R1-02	71	C	3	1	10	13	5.12	5.15	Serpentinized harzburgite	-	-
71C-5R1-01	71	C	5	1	20	23	7.58	7.61	Serpentinized harzburgite	-	-
71C-6R1-03.3	71	C	6	1	70	74	10.33	10.37	Dolerite	-	-
69A-5R1-01.3	69	A	5	1	137	151	8.25	8.39	Metadolerite	inter. carb	cc*
69A-6R1-01	69	A	6	1	127	130	9.87	9.90	Metadolerite	-	-
69A-8R1-01	69	A	8	1	14	18	11.46	11.50	Metadolerite	inter. carb	cc*
69A-10R2-01	69	A	10	2	14	16	16.08	16.10	Serpentinized harzburgite	carb vein	arg
72B-6R1-01	72	B	6	1	15	18	7.86	7.89	Rodingitized gabbro	-	-
72B-6R1-02	72	B	6	1	66	68	8.37	8.39	Rodingitized dolerite	inter. carb	cc
72B-7R1-01	72	B	7	1	3	5	9.02	9.04	Talc/amphi./chlorite schist	inter. carb	cc*
72B-7R1-03	72	B	7	1	55	58	9.54	9.57	Talc/amphi./chlorite schist	inter. carb	cc*
72B-7RCC-01	72	B	7	CC	9	13	10.38	10.42	Rodingitized gabbro	-	-
72B-8R1-01	72	B	8	1	19	22	10.90	10.93	Serpentinised harzburgite	carb vein, repl. core	cc IIb
72B-8R1-02	72	B	8	1	69	72	11.40	11.43	Talc/amphi./schist & serp. harzburgite	carb vein, repl. core	cc IIb
72B-8R2-01	72	B	8	2	26	30	11.77	11.81	Serpentinized harzburgite	carb vein, repl. core	cc I, cc IIa, cc IIb
72B-8R2-02	72	B	8	2	50	51	12.00	12.02	Serpentinized harzburgite	repl. core	cc*, mg-cc*
72B-8R2-03	72	B	8	2	67	70	12.18	12.20	Serpentinized harzburgite	carb vein, repl. core	cc I, cc IIa, cc IIb
72B-8RCC-01.3	72	B	8	CC	0	5	12.28	12.33	Serpentinized harzburgite	repl. core	cc IIa, cc IIb
76B-3R1-01	76	B	3	1	78	83	4.22	4.27	Serpentinized dunite	-	-
76B-5R1-05	76	B	5	1	55	59	7.28	7.32	Serpentinized dunite	carb vein, repl. core	cc III, dol
76B-5R1-06	76	B	5	1	77	80	7.50	7.53	Metagabbro	carb vein, inter. carb	cc
76B-6R1-01	76	B	6	1	63	65	8.61	8.63	Serpentinized harzburgite	-	-
76B-6R1-02	76	B	6	1	118	122	9.16	9.20	Serpentinized harzburgite	carb vein	cc IIa, cc IIb
76B-7R1-01	76	B	7	1	60	62	10.32	10.34	Serpentinized harzburgite	-	-
76B-8R1-01	76	B	8	1	90	94	12.05	12.09	Serpentinized harzburgite	-	-
76B-8R1-02	76	B	8	1	112	117	12.27	12.32	Serpentinized harzburgite	carb vein	cc III, cc IIb, dol, mgs
76B-8R1-03	76	B	8	1	148	151	12.63	12.66	Serpentinized harzburgite	-	-
76B-9R1-01	76	B	9	1	5	9	12.92	12.96	Serpentinized harzburgite	carb vein	arg, cc III, cc IIb, dol, mgs
76B-10R1-03.3	76	B	10	1	91	111	15.50	15.70	Metagabbro	-	-
68B-1R1-01	68	B	1	1	10	13	0.10	0.13	Serpentinized harzburgite	carb vein	arg*
68B-4R1-01	68	B	4	1	84	87	4.84	4.87	Serpentinized dunite	-	-
68B-7R1-01.1	68	B	7	1	3	5	7.60	7.62	Serpentinized dunite	-	-

* Carbonate mineralogy based on optical and cathodoluminescence microscopy

arg = aragonite, cc = calcite, mg-cc = Mg-rich calcite, dol = dolomite, mgs = magnesite; carb vein = carbonates precipitated in veins, repl. core = carbonates replacing the cores of complete serpentinized olivine, inter. carb = interstitial carbonates

4 Results

4.1 Host Rocks

The carbonate veins are hosted in ultramafic, mafic, and clastic sedimentary rocks. Cores from the northwestern (M0071) and most eastern sites (M0068) contain varying proportions of ultramafic-, mafic and sedimentary domains that have been interpreted as originating from mass-wasting and local faulting processes (Früh-Green et al., 2017; Rouméjon, Früh-Green, et al., 2018). Ultramafic and mafic host rocks were recovered from the central part of the southern wall (IODP Sites M0069, M0072, M0076) and are described as *in-situ* portions of the AM indicated by coherent, decimeter- to meter-long sections of cores, as well as consistent structural measurements (Früh-Green et al., 2017, 2018) (Figure 2 and 3a-c). The central sites also make up the deepest boreholes, and the following discussion mainly focuses on observations from these cores.

Modal proportions of primary minerals in the peridotites range from 60 % – 100 % olivine, 0 % – 40 % pyroxene (including minor clinopyroxene), and <1 % – 2 % spinel (Rouméjon, Früh-Green, et al., 2018), however some serpentinized peridotites from Site M0072 have as much as 5 to 8 vol% magnetite and differ considerably from other typical ultramafic domains (Figure 3a). Metamorphosed gabbroic and doleritic intrusions are largely altered to tremolite, chlorite, and/or talc, which locally overprint the serpentinization textures. The ultramafic samples are characterized by complex networks of distinct generations of carbonate veins filled with aragonite, calcite, dolomite and/or magnesite.

4.2 Carbonate occurrences

Carbonates in the basement of the southern wall occur as (i) interstitial carbonates, (ii) carbonates replacing fully serpentinized olivine cores, and (iii) carbonate veins (Table 1 and Figure 2). Carbonate veins were observed in both mafic and ultramafic rocks. Interstitial carbonates were only observed in mafic rocks, and carbonates in olivine cores were only found within serpentinized peridotites. Interstitial carbonates are typically found in metadolerites, talc-amphibole ± chlorite schists and metagabbro. Calcite is the only carbonate phase and has grain sizes < 20 µm, except for one metagabbro with carbonate grains < 0.1 mm (Figure 3b and d). Interstitial carbonates are limited to the central sites at the southern wall (M0069, M0072, M0076). Carbonates replacing the core of olivine are dominantly calcite and rarely dolomite and have an average grain size < 50 µm

(Figure 3e - f). Calcite within the crystal cores is restricted to Site M0072 and can occur as one or two generations in the same sample, whereas dolomite is limited to samples from Site M0076.

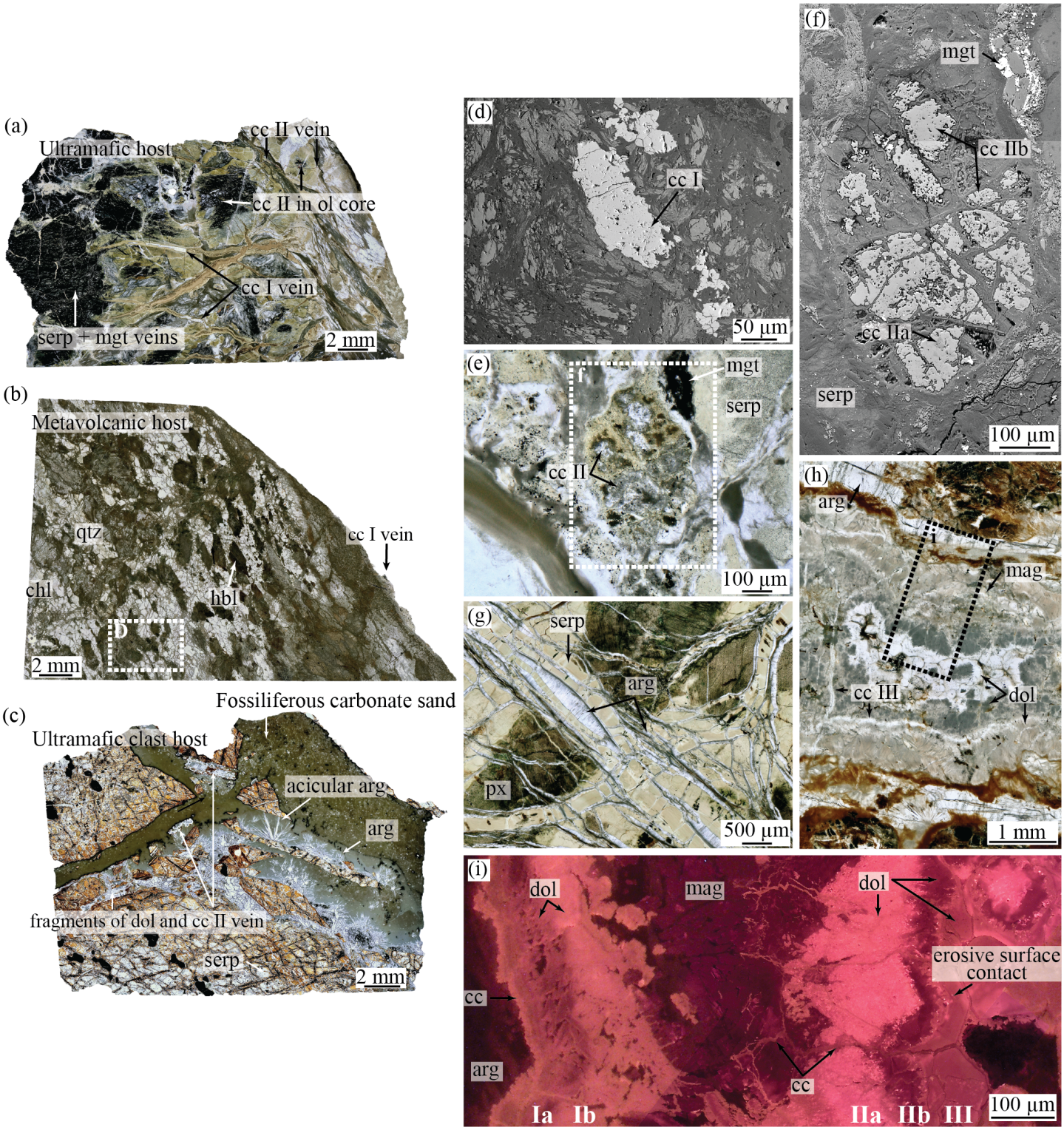

Figure 3. Characteristic petrologic features of host lithologies and carbonates. (a) Thin section scan of fully serpentinized harzburgite with increased magnetite content, calcite I and II veins, and calcite II in olivine cores. Two calcite I veins are cut by later serpentinite vein (72B_8R_2_67-69.5). (b) Thin section scan of metagabbroic host rock with calcite I vein and interstitial calcite I (76B_5R_1_77-80, close-up in Fig. 3d. (c) Thin section scan of fully serpentinized dunite clast hosting fragments of dolomite and calcite II veins, and aragonite with acicular growth within the fossiliferous carbonate sand (71A_1R_1_45-48). (d) Interstitial calcite in metagabbroic sample from Fig.3b (BSE image). (e) Calcite II replaced fully serpentinized olivine (PPL, 72B_8R_CC_0-5, close-up in Fig. 3f). (f) Calcite IIa and IIb in olivine core (BSE image). (g) A network of fibrous aragonite veins crosscut all other textures in the ultramafic host rock (PPL, 69A_10R_2_14-16). (h) Overview of a multigeneration dolomite vein in the ultramafic rock crosscut by later calcite III (PPL, 76B_9R_1_5-9, close-up in Fig. 3i). (i) CL-image of the dolomite vein of Fig. 3h containing multiple generations of dolomite, marked by Roman numerals, and other carbonate phases. Abbreviations: Arg, aragonite; cc, calcite; chl, chlorite; dol, dolomite; hbl, hornblende; mgs, magnesite; mgt, magnetite; serp, serpentine; qtz, quartz.

4.2.1 Carbonate veins

Veins are the most abundant carbonate occurrence in the Atlantis Massif basement and tend to be concentrated in the central drill sites closest to the LCHF (M0069, M0072, M0076) (Figure 2). The carbonate veins typically dissect grain boundaries, have kinked to irregular shapes, and show crosscutting or more rarely branching geometries. They are less than 1 cm wide and are mainly hosted by variably serpentinized peridotites and crosscut most other textures, indicating a late formation stage (Figure 3g, 4a). The abundance of carbonate veins is highly variable and can be as low as one vein or make up to half of a hand sample (~ 40 vol%) as in some ultramafic rocks from Site M0076. The veins are composed of aragonite, calcite, dolomite and magnesite in variable proportions.

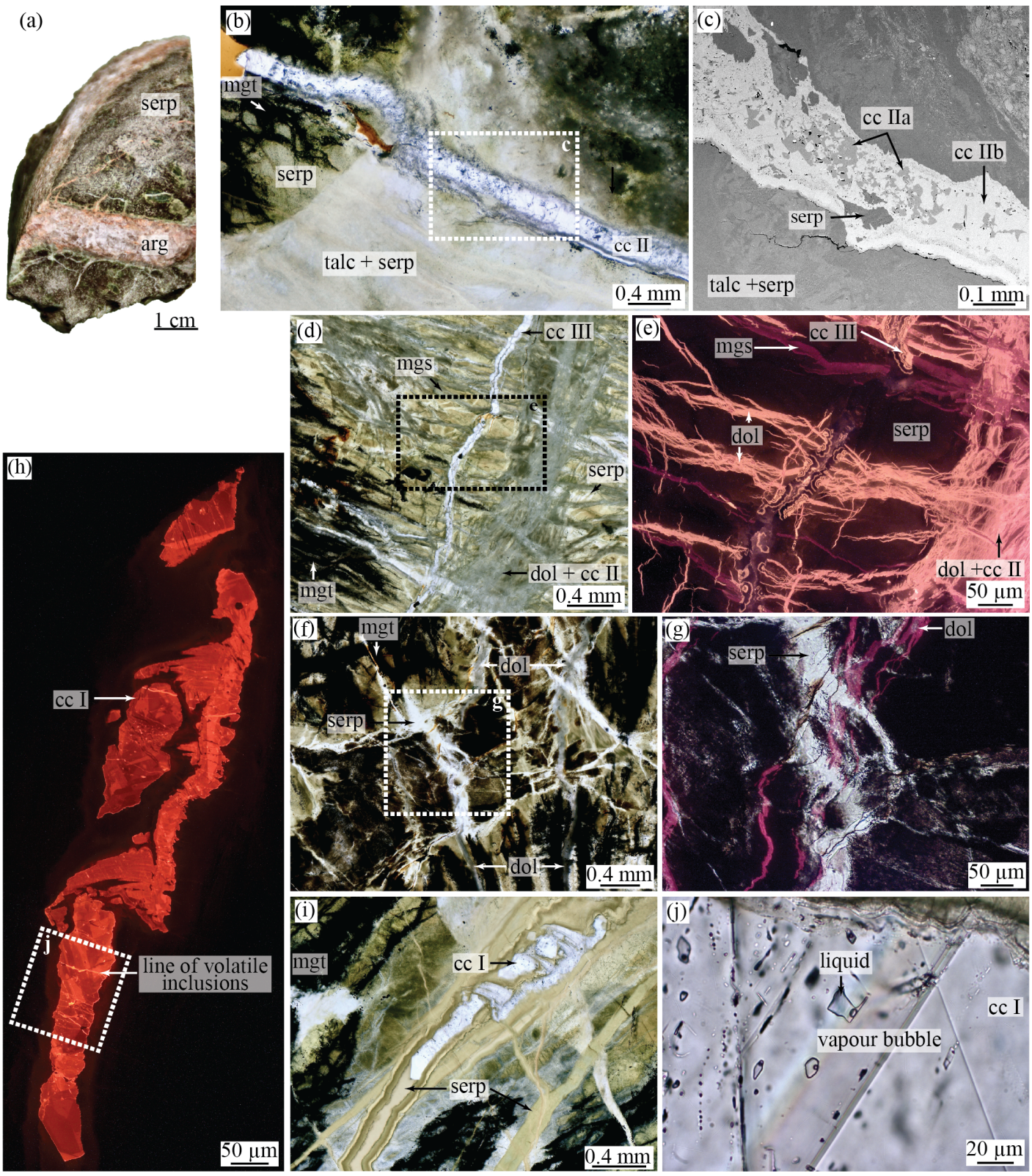
(a)
serp
arg
1 cm
(b)
mgt
serp
c
talc + serp
cc II
0.4 mm
(c)
cc IIa
cc IIb
serp
talc +serp
0.1 mm
(d)
cc III
mgs
e
serp
mgt
dol + cc II
0.4 mm
(e)
mgs
cc III
dol
serp
dol +cc II
50 µm
(h)
cc I
j
line of volatile inclusions
50 µm
(f)
mgt
dol
serp
g
dol
0.4 mm
(g)
dol
serp
50 µm
(i)
mgt
cc I
serp
0.4 mm
(j)
liquid
cc I
vapour bubble
20 µm

Figure 4. Sample pictures and photomicrographs of carbonates. (a) Late microcrystalline aragonite vein in serpentinized harzburgite (76B_9R_1_70-73). (b) Calcite II vein in serpentinized dunite (PPL, 72B_8R_2_26-30, close-up in Fig. 4c). (c) Calcite IIa + IIb vein with straight crystal contacts from Fig. 4b (BSE image). (d) A network of magnesite, dolomite and calcite II veins cut by radial growth calcite III (PPL, 76B_8R_1_112-117). (e) CL- image of the carbonate network of Fig. 4d. (f) Dolomite veins in serpentinized harzburgite crosscut by serpentine veins (PPL, 76B_5R_1_55-59, close-up in Fig. 4g). (g) Dolomite vein crosscut by serpentinite from Fig. 4f (PPL + CL). (h) CL- image of highly deformed calcite I vein with several lines of secondary fluid inclusions of Fig. 4i (72B_8R_2_26-30, close-up in Fig. 4j). (i) Calcite I vein in serpentinized dunite of Fig 4h (PPL). (j) Multiple secondary fluid inclusions in calcite I vein with small vapour phases of Fig. 5h (PPL). Abbreviations: Cc, calcite; dol, dolomite; mgs, magnesite; mgt, magnetite; serp, serpentine.

In half of the samples, at least two generations of carbonates coexist in the same vein, whereby two samples 76B_8R_1_112-117 and 76B_9R_1_5-9 show at least four different generations (Figure 3h - i, 4b - c, and 5). The altered mafic rocks are devoid of carbonate veins, except for sample 76B_5R_1_77-80 that contains a narrow (< 50 µm) vein of calcite on the outside of the sampled rock piece (Figure 3b). Serpentinites show the highest textural variability of carbonate veins at the AM.

Magnesite, dolomite, and calcite veins are a few mm wide (Figure 3a, h - i, and 4b - i) and occur mainly at the central Sites M0072 and M0076, except for one calcite/dolomite vein, found in a sedimentary breccia on top of Hole M0071A (71A_1R_1_45-48, Fig. 3c). Magnesite veins are the least frequent, occurring exclusively in association with dolomite and limited to the deeper sections of Hole M0076B (> 12 mbsf). Crosscutting relationships indicate that most magnesites pre-date all other carbonates (Figure 4d - e). Dolomite veins are more common at Site M0076; they are < 5 mm wide and precipitated at the rim of multiphase veins or are cut by serpentine + magnetite veins, suggesting an early stage of formation (Figure 3h - i, 4f - g). They differ from the other veins in that they are sometimes formed by multiple generations of dolomite with partly dissolved surfaces and pitted textures (Figure 3i and 5).

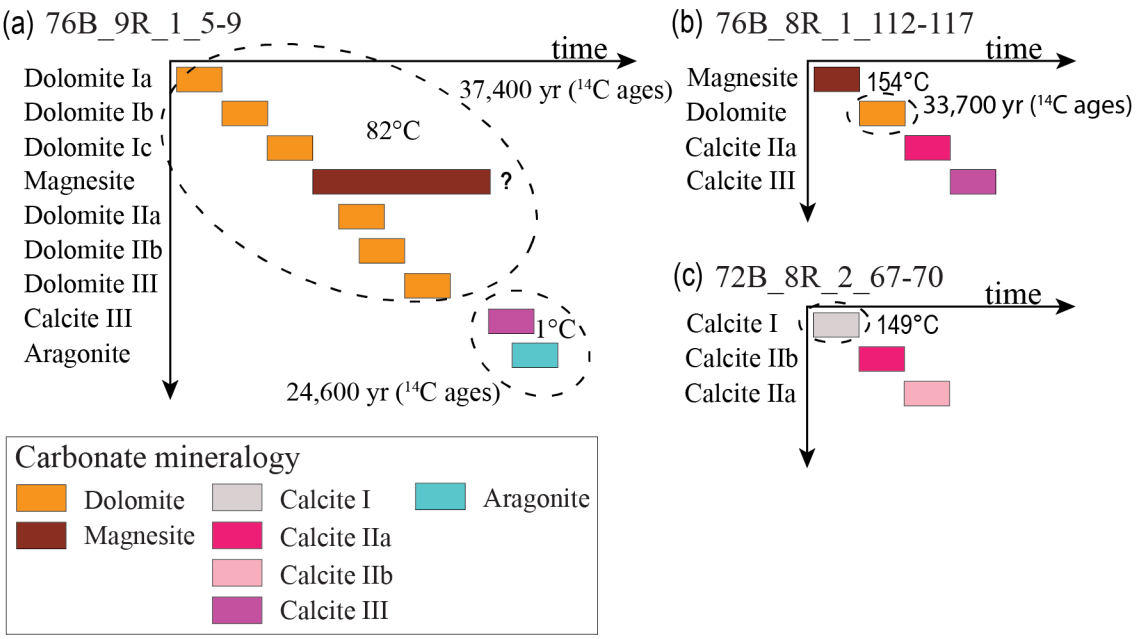

329

330 **Figure 5.** Simplified time log of carbonate vein formation of (a) 76B_9R_1_5-9, (b)
331 76B_8R_1_112-117 and (c) 72B_8R_2_67-70, based on cold cathodoluminescence microscopy.
332 The Roman numerals (I to III) indicate different generations, letters (a to c) indicate a change in
333 chemical composition or texture. Different generations occur intergrown, with erosive surface
334 contacts or straight crystal contacts; clumped isotope temperatures of carbonate formation and
335 radiocarbon age data from Ternieten et al. (in prep.).

336

337 Calcite veins are most common at Site M0072, showing the highest textural variability,
338 and often occur as two distinct generations within the same vein. At Site M0072, they constitute
339 the earliest carbonate generation with intergrown or straight crystal contacts to the surrounding
340 minerals (Figure 4b - c). Locally calcite veins are intergrown with serpentine; these are highly
341 deformed and exhibit secondary fluid inclusions, suggesting an earlier formation stage (Figure 3a,
342 4h - j). The fluid inclusions are composed of an aqueous liquid and a small vapour phase suggesting
343 formation temperatures below 100°C. These veins are limited to the deeper section (> 11 mbsf)
344 at Hole M0072B. In two samples from Site M0076 (76B_5R_1_55-59, 76B_8R_1_112-117),
345 calcite shows botryoidal textures (Figure 4d - e), which is indicative of growth in open fractures.

346 The most abundant and volumetrically dominant carbonate type are up to 1 cm wide
347 aragonite veins that are observed throughout the ultramafic rocks at Hole M0069A, in the deeper
348 section of Hole M0076B (> 13 mbsf), in the top cores from Holes M0071A and M0068B, and on
349 the altered surface of a deeper sample from Hole M0068B (Figure 2). The aragonite veins crosscut
350 the primary rock fabric (Figure 3g and 4a), also postdate all secondary fabrics and are the last to
351 be formed. Vein aragonite displays three distinct crystal habits: fibrous crystals, acicular crystals,
352 and microcrystalline aragonite (Figure 3c and g, and 4a). The long axes of acicular crystals
353 growing into open spaces and the fibrous crystals are preferentially oriented vertical to the walls
354 of the veins.

355 4.3 Carbonate chemistry

356 A significant observation in the basement rocks is the high variability in composition and
357 distribution of carbonate phases and the presence of distinct generations of carbonates within one
358 sample and/or vein at Holes M0072B and M0076B. The carbonates have distinctly different Fe,
359 Mn, Sr and Mg concentrations which allow distinguishing different generations and indicate local
360 variations in fluid chemistry. Representative chemical analyses of all carbonate phases are
361 presented in Table 2.

362 Carbonates in the altered mafic rocks exhibit a limited range of major element
363 compositions. Interstitial calcites have negligible MgO, and FeO and MnO concentrations that
364 vary from 0 to 0.3 wt% and from 0 to 0.1 wt%, respectively. The single identified calcite vein
365 within the mafic rock samples only differs slightly by higher MgO concentration of 2.4 to 3.2 wt%,
366 but also shows FeO and MnO concentration < 0.1 wt% (Table 2). In contrast, the carbonates within
367 the serpentinized ultramafic rocks show greater textural and chemical variations. Magnesite veins
368 have FeO concentrations ranging from 0.6 to 1.3 wt% and MnO concentrations from 2.4 to 4.1
369 wt% (Fig. 6a - b). These FeO and MnO patterns are within the range of dolomite and calcite
370 compositions. The dolomite veins have slightly more variable FeO and MnO concentrations
371 compared to magnesite and lower FeO compared to calcites (FeO = 0 to 0.9 wt%, MnO = 0 to 6.0
372 wt%, Fig. 6a - b). Sample 76B_9R_1_5-9, which contains a multiphase dolomite vein (Figure 3h
373 - i), has distinctly higher MnO contents at the rim compared to the centre (MnO_{rim} = 6.0 wt%,
374 MnO_{centre} = 3.0 wt%; Fig. 6b).

Table 2. Representative analyses of carbonate in ultramafic and mafic rocks from the southern wall at the Atlantis Massif.

Sample	76B_5R_1, 77-80	76B_5R_1, 77-80	69A_10R_2, 14-16	72B_8R_1, 69-72	72B_8R_1, 69-72	72B_8R_2, 67-70	72B_8R_2, 67-70	72B_8R_2, 26-30	76B_9R_1, 5-9	76B_9R_1, 5-9	76B_5R_5, 55-59	76B_9R_1, 5-9
Hole	M0076B	M0076B	M0069A	M0072B	M0072B	M0072B	M0072B	M0072B	M0076B	M0076B	M0076B	M0076B
Host rock	Mafic	Mafic	Ultramafic	Ultramafic	Ultramafic	Ultramafic	Ultramafic	Ultrmafic	Ultamafic	Ultramafic	Ultramafic	Ultramafic
Phase	Calcite	Calcite	Aragonite	Calcite IIb	Calcite IIb	Calcite IIa	Calcite IIa	Calcite I	Calcite III	Dolomite	Dolomite	Magnesite
Occurrence	Vein	Interstitial	Vein	Vein	Repl. core	Vein	Repl.core	Vein	Vein	Vein	Repl.core	Vein
(wt%)												
SiO_2	0.01	0.03	0.00	0.00	0.00	0.00	0.00	0.00	0.00	0.00	3.15	0.10
MgO	2.78	0.04	0.00	0.20	1.52	14.72	14.84	0.03	4.42	20.41	20.27	44.03
Al_2O_3	0.01	0.02	0.00	0.01	0.00	0.00	0.00	0.00	0.00	0.00	0.06	0.00
BaO	0.00	0.05	0.00	0.00	0.00	0.00	0.01	0.01	000	0.00	0.00	0.00
FeO_{tot}	0.09	0.21	0.00	0.07	0.34	1.23	1.07	0.12	0.02	0.17	0.58	0.64
MnO	0.00	0.05	0.00	0.93	1.42	4.71	4.00	0.01	2.06	3.43	1.96	4.04
SrO	0.06	0.07	0.52	0.00	0.00	0.01	0.01	0.03	0.06	0.00	0.01	0.00
CaO	52.64	55.61	55.23	54.89	52.65	33.16	33.91	55.86	48.93	28.86	26.84	0.11
CO_2	44.42	43.93	44.25	43.90	44.06	46.17	46.16	43.94	44.51	47.13	47.13	51.09
Total	100	100	100	100	100	100	100	100	100	100	100	100

Abbreviation: repl. core = carbonates replacing cores of complete serpentinized olivines

The calcite veins show pronounced variations in Mg, Fe and Mn and, in combination with petrographic observations, can be classified into three groups. Calcite I is almost pure $CaCO_3$; it constitutes the earliest carbonate phase and the only phase where we observed fluid inclusions (see section 4.2.1). They have low SrO, MgO, FeO and MnO concentrations of < 0.2 wt%, which is similar to the interstitial calcites observed within the mafic rocks and distinguish them from other calcites within the ultramafic lithologies (Figure 7a and c). The most common calcites, especially at Site M0072, are classified as calcite II. Two subgroups can be distinguished based on the Mg concentration: Calcite IIa with MgO > 11.9 wt%, and calcite IIb with MgO < 7.3 wt%. FeO and MnO contents vary from 0 to 3.3 wt% and from 0 to 7.3 wt%, respectively (Figure 7a - d). Calcite IIa also shows higher Fe and Mn concentrations than calcite IIb in some samples at Site M0072, whereas such distinct variations between the subgroups were not observed at Site M0076. The subgroups show no unique chronology, and depending on the location, either calcite IIa or calcite IIb represents the earlier phase. Calcite III veins are defined by concentrations of MgO of 2.2 to 6.3 wt%, FeO of < 0.2 wt%, and a wide range of MnO contents from 0 to 3.6 wt%. They are limited to Site M0076 and are the more common calcite type at this site where they represent the last or one of the latest carbonate phases, often occurring within open fractures as botryoidal crystals (Figure 4d - e, 5 and 7b and d). Aragonites throughout all cores have uniform compositions with MgO and MnO below the detection limit, only minor FeO concentrations < 0.1 wt% and variable to high SrO concentrations (0.4 - 2.5 wt%, Table 2). In comparison, all other carbonate phases have SrO concentrations of less than 0.2 wt%.

The major element patterns of carbonates replacing fully serpentinized olivine cores are indistinguishable from the vein carbonates. Calcite IIa and IIb that replace olivine and/or serpentine show Fe and MnO contents from 0.2 to 2.0 wt% and 0.8 to 7.3 wt%, respectively, with calcite IIa showing the highest MnO concentrations (> 2.7 wt%). This is similar to calcite IIa in the veins; however, a distinct separation between the calcite subgroups based on their FeO content cannot be made (Figure 7e - f). No calcite I or calcite III were identified replacing olivine cores and or serpentine. The dolomites replacing olivine have a uniform and much lower manganese concentrations than the replacive calcites (MnO = 1.7 to 2.3 wt%). FeO contents vary from 0.4 to 1.1 wt%, which is within the same range as dolomite occurring in veins (Table 2).

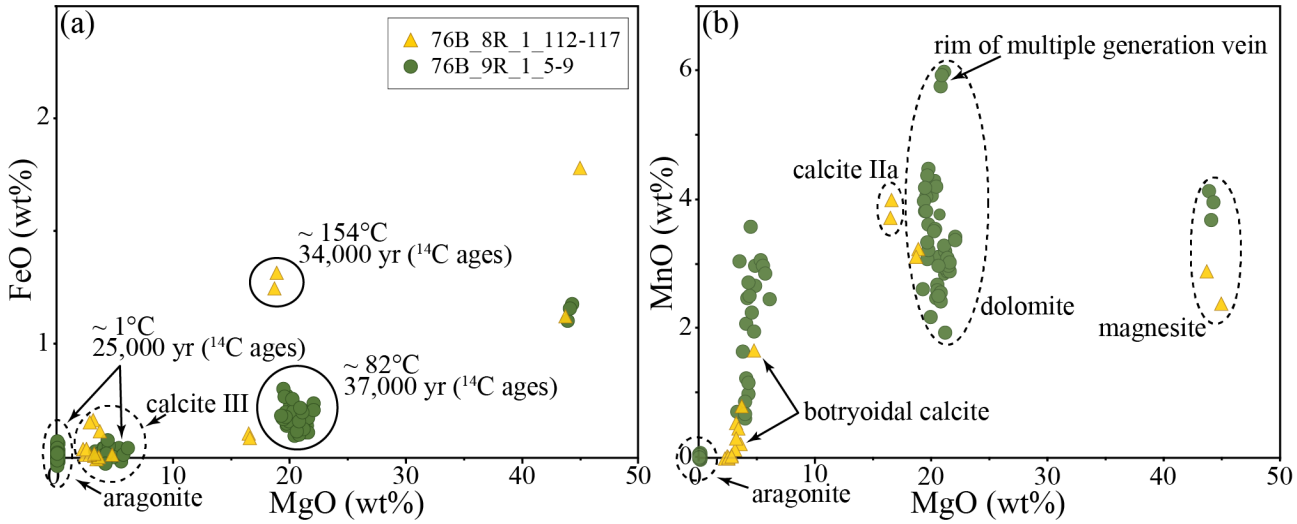

405

406 **Figure 6.** Variations in (a) FeO versus MgO content and (b) MnO versus MgO content of
407 carbonate veins hosted by serpentinized peridotites from two samples of Hole M0076B from the
408 southern wall at the Atlantis Massif (76B_8R_1_112-117, 76B_9R_1_5-9). The ultramafic rocks
409 show a diverse assemblage of carbonate phases in one sample (aragonite, calcite, dolomite,
410 magnesite). Pictures of the samples in Fig. 3h and i, and Fig. 4d and e. Clumped isotope
411 temperatures of carbonate formation and radiocarbon age data from Ternieten et al. (in prep).

412

413 4.3.1 Carbonate generations

414 Cathodoluminescence (CL) in carbonates results from trace-element substitution for Ca^{2+}
415 and Mg^{2+} and is the most suitable method to identify different carbonate generations with only
416 minor chemical variations. Although various trace elements are capable of influencing carbonate
417 CL (Machel, 1985), the ion Mn^{2+} is the most critical "activator", and Fe^{2+}, Fe^{3+}, Ni^{2+}, and Co^{2+} are
418 common "quenchers" (Götze, 2012). The intensity and colour of luminescence are dependent on
419 the relative proportions of Mn and Fe (Barnaby & Rimstidt, 1989). Additionally, the stimulated
420 luminescence bands depend on the position in the crystal structure in which the Mn^{2+} ion is
421 integrated (Mg^{2+} or Ca^{2+} position) (Götze, 2012). Thus, the same MnO content can result in
422 different CL. This is particularly well illustrated in Figure 5, which shows simplified time logs of
423 carbonate vein formation of three different samples based on CL investigations. Six carbonate
424 generations with dolomite, magnesite, calcite III, and aragonite (Figure 5a) were identified in

Sample 76B_9R_1_5-9 (Figure 3h - i). Dolomite is characterized by multiple generations within a single vein, and we identified three generations with partial dissolution and pitted textures between them and separated by magnesite precipitation. Dolomite veins from this sample showed significant variations in the MnO content (MnO_{dol} = 1.9 to 6.0 wt%) and only a limited range of FeO from of 0.1 to 0.3 wt%, which makes variations in Mn^{2+} concentration the most likely cause for the differences in luminescence (Figure 6a - b). Sample 76B_8R_1_112-117 (Figure 4d - e) contains four different generations with magnesite, dolomite, calcite IIa and calcite III (Figure 5b). Similar to sample 76B_9R_1_5-9, dolomite is the volumetrically dominant carbonate phase in this sample; however, the vein network is much finer, and no distinct generations within the dolomite can be identified. This coincides with homogeneous MnO and FeO content of the dolomite (Figure 6a - b). However, both samples show a decrease in the FeO content with time from 0.6 to 1.0 wt% in the earliest generations of magnesite to < 0.1 wt% in the latest aragonites and calcite III. Sample 72B_8R_2_67-70 (Figure 3a) is representative for Hole M0072B and contains three generations of calcite: calcite I, calcite IIa, calcite IIb (Figure 5c). The different generations observed by CL are also reflected by distinct major element compositions (Figure 7a and c). In addition, calcite IIa and IIb show a decreasing FeO content with time from $FeO_{cc\ IIa}$ = 1.2 wt% to $FeO_{cc\ IIb}$ = 0.3 wt%, similar to samples from Hole M0076B.

Figure 7. Variations in FeO and MnO versus MgO content of calcite veins hosted by serpentinized peridotites from the southern wall at the Atlantis Massif of (a and c) Hole M0072B and (b and d) Hole M0076B, and of carbonates replacing fully serpentinized serpentine olivine cores from Hole M0072B (e and f). Clumped isotope temperatures of carbonate formation from Ternieten et al. (in prep). The dashed lines mark the difference between calcite IIa and IIb. Black symbols in figure (e and f) represent the chemical composition of calcite veins from the same sample.

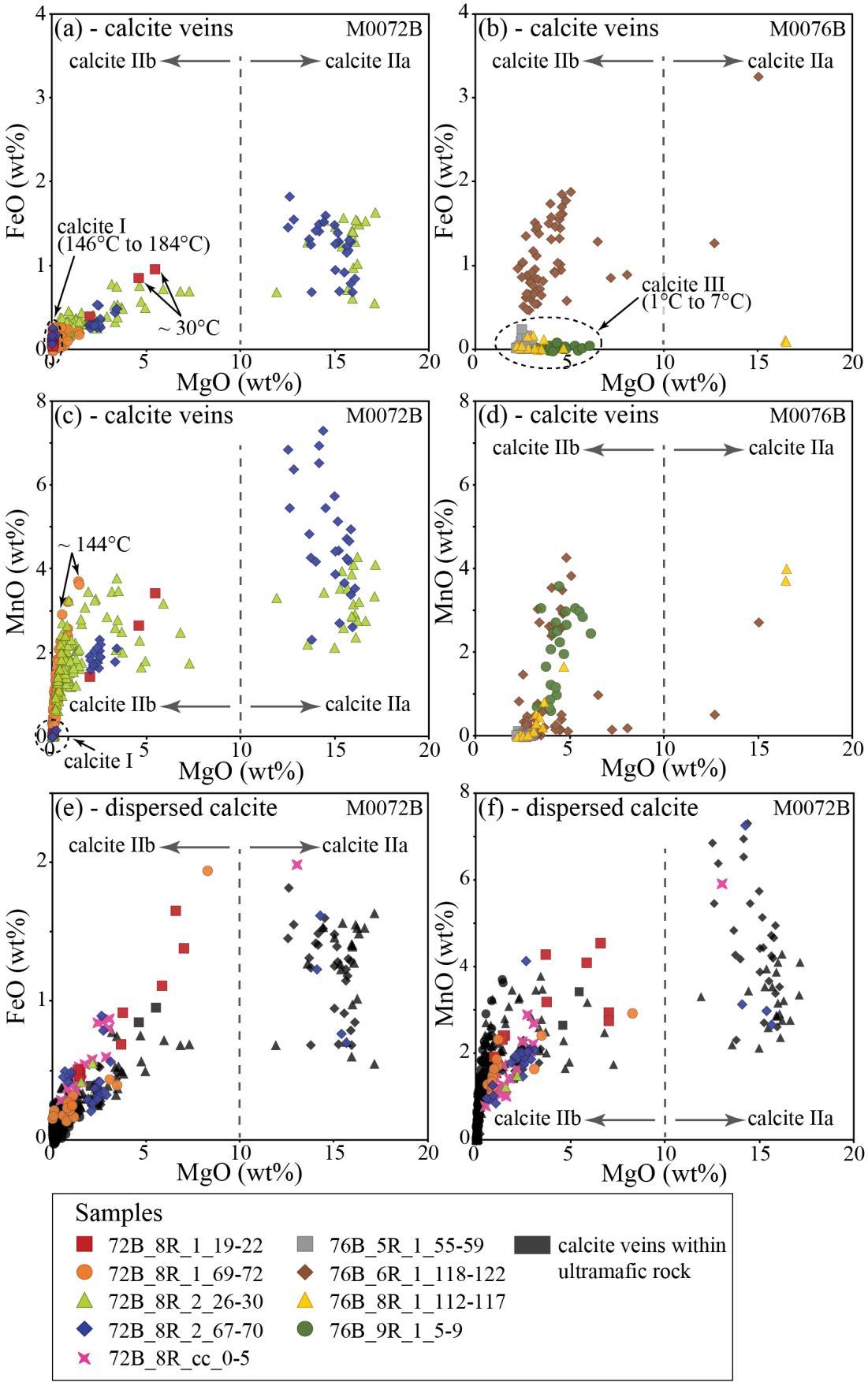
(a) - calcite veins
M0072B
calcite IIb
calcite IIa
calcite I
(146°C to 184°C)
~ 30°C
FeO (wt%)
MgO (wt%)
(b) - calcite veins
M0076B
calcite III
(1°C to 7°C)
(c) - calcite veins
M0072B
~ 144°C
calcite I
MnO (wt%)
(d) - calcite veins
M0076B
(e) - dispersed calcite
M0072B
(f) - dispersed calcite
M0072B
Samples
72B_8R_1_19-22
72B_8R_1_69-72
72B_8R_2_26-30
72B_8R_2_67-70
72B_8R_cc_0-5
76B_5R_1_55-59
76B_6R_1_118-122
76B_8R_1_112-117
76B_9R_1_5-9
calcite veins within ultramafic rock

5 Discussion

Carbonation reactions in serpentinized peridotites are controlled by temperature, protolith composition and activities of dissolved constituents, and are particularly influenced by fluctuations in $a\mathrm{SiO_{2(aq)}}$ and $a\mathrm{CO_{2(aq)}}$. Figure 8 shows two activity-activity diagrams depicting phase relations in the $\mathrm{MgO\text{-}CaO\text{-}SiO_2\text{-}H_2O\text{-}CO_2}$ system. It has long been recognized that serpentinized peridotites are highly reactive in the presence of dissolved $\mathrm{CO_2}$ (Johannes, 1967, 1969), and with increasing $a\mathrm{CO_{2(aq)}}$, the characteristic alteration assemblage of serpentine + brucite will successively be replaced by serpentine + magnesite, followed by talc+magnesite and finally quartz + magnesite (Figure 8a) (e.g., Boschi et al., 2009; Hansen et al., 2005). Even at low temperatures, moderate concentrations of $\mathrm{CO_{2(aq)}}$ are sufficient to dissolve brucite in favour of carbonate. Thermodynamic models and experimental studies show that the $a\mathrm{SiO_{2(aq)}}$ and $a\mathrm{CO_{2(aq)}}$ are intimately linked and will ultimately affect silicate mineral stabilities, Mg/Ca ratios in the fluids and thus the composition of the precipitating carbonate (e.g., Frost & Beard, 2007; Grozeva et al., 2017; Hövelmann et al., 2011). Low $a\mathrm{Mg^{2+}}$ will favour the precipitation of calcite, whereas high concentrations of $\mathrm{CO_2}$ and $\mathrm{Mg^{2+}}$ in the fluids will favour dolomite and magnesite precipitation (Figure 8) (Grozeva et al., 2017).

Altered peridotites were recovered in all seven holes drilled across the AM southern wall. The exceptional core recovery preserved multiple carbonate generations that allow the reconstruction of the alteration history. One of the most remarkable features is the high variability in composition and distribution of carbonate phases, including magnesite, dolomite, calcite and aragonite. The diverse carbonate phases record progressive fluid infiltration and alteration during extension, unroofing and uplift of the AM and the simultaneous evolution from pervasive- to localized serpentinization. Figure 9 shows an interpretative cross-section of the Atlantis Massif, highlighting the most critical processes affecting alteration and carbonate formation of the oceanic core complex. Previous studies (e.g., Boschi et al., 2006; Karson et al., 2006; Rouméjon, Früh-Green, et al., 2018) showed that the alteration of the AM is affected by seawater infiltration via grain boundary flow and a complex network of steeply dipping normal faults. Fluids are focused along the detachment fault zone and discrete ductile shear zones triggering serpentinization and silica metasomatism of serpentinites and gabbros, resulting in talc-amphibole-chlorite schist lenses. Different carbonate occurrences are characteristic for different locations within the AM and timing during its uplift. Black squares within Figure 9 indicate locations that are recorded by

482 samples from the different drill holes. A conceptual model for the hydrothermal evolution of the
483 AM is presented in Figure 10, which summarizes the alteration history of the peridotites that are
484 in proximity to mafic intrusions (Figure 10.1 - 10.3) compared to those in the periphery to
485 intrusions (Figure 10.4 - 10.6). Our model follows work of Rouméjon and Cannat (2014), who
486 argued that the combination of anisotropic thermal contraction and tectonic stresses in the brittle
487 domain of the mantle leads to pervasive micro-fracturing of peridotites at mid-ocean ridges. This
488 provides an efficient permeability network of pathways for serpentinization and initial carbonate
489 precipitation.

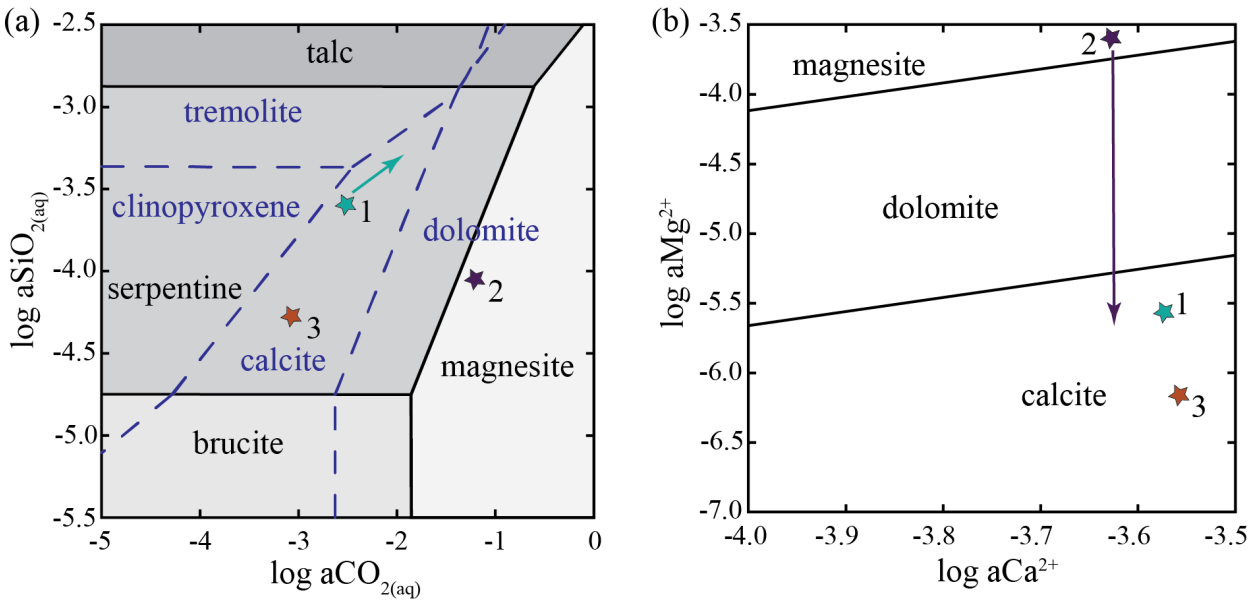

490

491 **Figure 8.** Activity-activity diagrams depict phase relations in the MgO-CaO-SiO_2-H_2O-CO_2
492 system at 300°C and 35 MPa modified after Grozeva et al. (2017). Numbered stars indicate
493 potentially compositions of fluids from the three central sites representing distinct alteration
494 conditions at the Atlantis Massif; 1 = strong influence of mafic intrusion (M0072B), 2 = minor
495 influence of mafic intrusion (M0076B), 3 = alteration of abyssal peridotites (M0069A). (a) The
496 plot of log $a\mathrm{SiO_{2(aq)}}$ vs log $a\mathrm{CO_{2(aq)}}$ showing the stability fields of various silicate minerals and
497 carbonates. Continuous lines denote equal activities of phases in the MgO-H_2O-CO_2 system.
498 Dashed blue lines indicate equal activities of phases in the MgO-CaO-H_2O-CO_2 system. The Fluid
499 composition of M0072B moved to higher $a\mathrm{SiO_{2(aq)}}$ and $a\mathrm{CO_{2(aq)}}$ values over time. (b) The plot of
500 log $a\mathrm{Mg^{2+}}$ vs log $a\mathrm{Ca^{2+}}$. The fluid composition of M0076B moved out of the stability field of

magnesite and into the stability field of calcite with successively uplift and alteration of the AM. Reprint from Grozeva et al. (2017), Copyright 2017, with permission from Elsevier.

5.1 Alteration heterogeneities along the southern wall of the Atlantis Massif

Our detailed petrological, textural and geochemical observations point to three main controlling factors that affect carbonate precipitation at the Atlantis Massif: (i) fluid composition and flux, (ii) temperature of the system, and (iii) presence of mafic intrusions. We focus on the three central sites (M0069, M0072, M0076), each of which provides distinct pieces of information about the complex history of fluid infiltration and alteration during exhumation of the massif.

5.1.1 Carbonate formation in the presence of mafic intrusions

Interlayers of mafic intrusions are most prevalent at Hole M0072B, which shows the highest degree of silica metasomatism, marked by talc-, amphibole- and chlorite-rich domains, and which provides the best information about the influence of mafic intrusions on fluid and carbonate chemistry. This hole is characterized by a lack of magnesite and dolomite in the ultramafic rocks, which suggest that Mg^{2+} transport was strongly limited in the proximity of the metasomatic interlayered mafic intrusions and was locked into other silicate alteration assemblages (Figure 10, frame 1 - 3).

At Hole M0072B, the initial carbonate phase is calcite I, which formed syn-serpentinization and is intergrown with serpentine in veins (Figure 10.2). The lack of magnesite and dolomite suggests that removal of Mg^{2+} resulted in low Mg/Ca ratios and favoured calcite precipitation (Figure 8b) (e.g., Hövelmann et al., 2011; Lumsden et al., 1995; Peuble, Godard, et al., 2015). Alteration of mafic intrusions and an associated static replacement of serpentine by talc has been previously identified at the Atlantis Massif (Boschi et al., 2006; Rouméjon, Früh-Green, et al., 2018). Talc formation can result from either Si-addition to or Mg-removal from the serpentinized peridotite. Previous studies (Bach et al., 2004; Boschi et al., 2006; Rouméjon, Früh-Green, et al., 2018) assumed that Si-addition rather than Mg-removal is responsible for talc formation, given that the alteration of mafic rocks releases significant amounts of silica compared with ultramafic rocks (Malvoisin, 2015; Wetzel & Shock, 2000). The metasomatism of gabbro and dolerites in the peridotites provide a source of Ca^{2+} and SiO_2 from the dissolution of plagioclase

and pyroxenes and removal of Mg^{2+} through talc formation (Berndt et al., 1989; Bischoff & Dickson, 1975). In an experimental study at 400°C, Allen and Seyfried (2003) showed that high-temperature alteration could lead to a faster dissolution of clinopyroxene compared to olivine, providing an additional input of SiO_2 and Ca^{2+} and lower input of Mg^{2+}. Elevated temperatures in the subsurface of the Atlantis Massif are indicated by the oxygen isotope composition of serpentine ($\delta^{18}O_{recrystallized\ serp}$ = 1.6 to 2.9 ‰, Rouméjon, Williams, et al., 2018) which correspond to formation temperatures between 320 and 360°C (assuming $\delta^{18}O_{fluid}$ = 2.4 ‰, Rouméjon, Williams, et al., 2018) and which would be sufficient for clinopyroxene dissolution. Calcite I veins yield one of the highest carbonate formation temperatures of all carbonates across the AM ($T_{\Delta 47}$ = 145 to 185 °C) and indicate that temperatures in the hydrothermal system remained high during later alteration. We propose that the hydrothermal fluid in proximity to silica metasomatism is depleted in Mg^{2+} and in combination with moderate aCO_2 and the dissolution of clinopyroxene with slower olivine serpentinization was sufficient to maintain low Mg/Ca ratios in the hydrothermal fluid and prevent magnesite and dolomite precipitation. Calcite I veins have MgO, FeO, and MnO concentrations below the detection limit, which distinguish them from other carbonates at the AM and suggests that all dissolved Mg^{2+}, Fe^{2+}, and Mn^{2+} was taken up by secondary silicate minerals (serpentine, talc, chlorite).

Calcite II is the second carbonate phase at Hole M0072B and occurs post-serpentinization within veins or replacing serpentine and/or olivine (Figure 10.3). Calcite II has higher MgO contents, which may be linked to an increase in Mg/Ca ratio resulting from an addition of unmodified seawater in the evolved hydrothermal fluids. A higher influx of seawater increase $CO_{2(aq)}$ and $Mg^{2+}_{(aq)}$ concentrations, shifting the equilibrium towards the Mg-carbonate stability fields (Figure 8a). This may also lead to faster dissolution rates of the primary minerals of the mafic and ultramafic rocks, which can add additional SiO_2, Mg^{2+} and Ca^{2+} to the fluids. Calcite II is separated into two subgroups, a Mg-rich calcite IIa and a Mg-poor calcite IIb (Figure 7). Calcite IIb precipitates from a fluid with lower $Mg^{2+}_{(aq)}$ concentration in areas where silica alteration minerals consumed more $Mg^{2+}_{(aq)}$ from solution. The Mg-rich calcite IIa precipitated from a fluid that was more influenced by serpentinization resulting in higher Mg^{2+} concentrations probably in more peripheral areas of the mafic intrusions. Some veins contain both calcite II subgroups, but without a clear chronology. This may reflect changes in the influence of the mafic intrusions on

560 the composition of the fluids over time, by either changes in the fluid pathway or variations in
561 dissolution and/or formation rates of primary and secondary minerals.

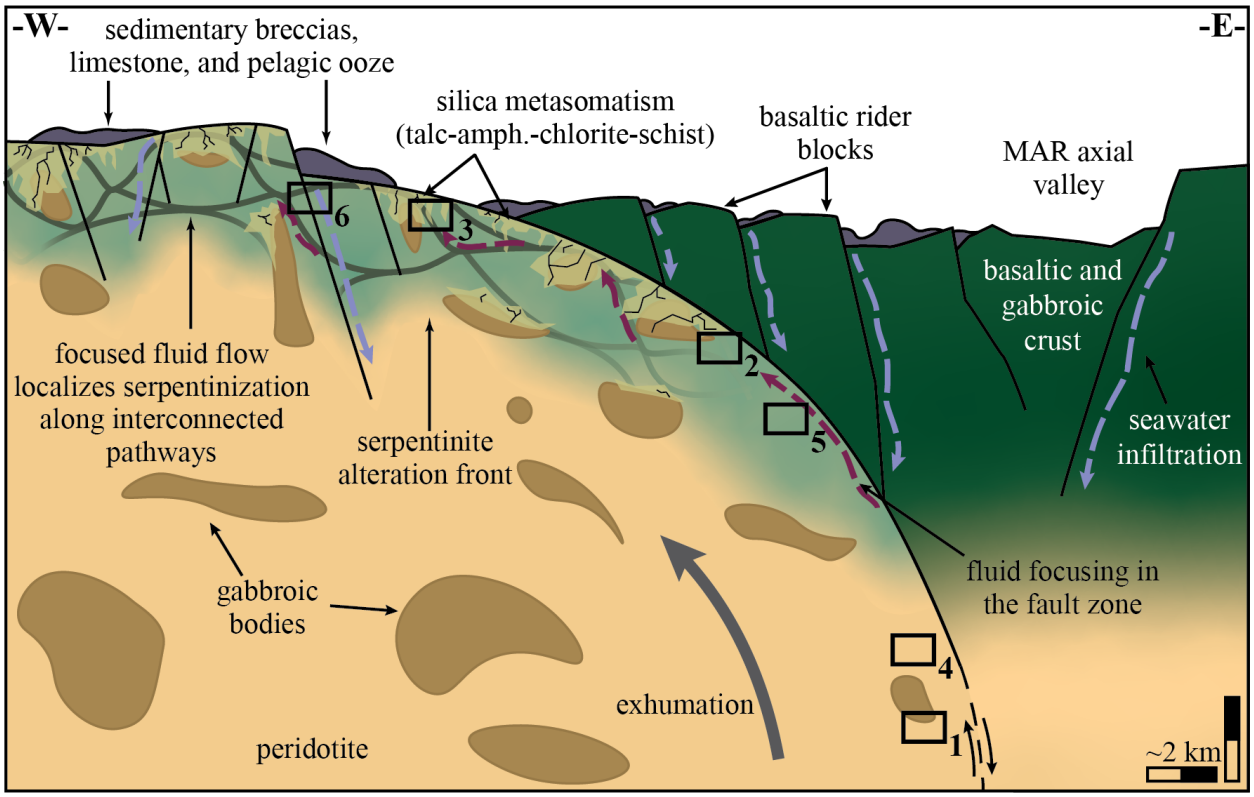

562

563 **Figure 9**. Interpretative cross-section of the Atlantis Massif, showing fluid pathways, metasomatic
564 zones, and extent and development of serpentinization (light green shaded region and lines) related
565 to detachment faulting and steep normal faults (modified after Karson et al., 2006, Boschi et al.,
566 2006, and Rouméjon et al., 2018). The oceanic core complex forms as a result of extension,
567 unroofing, and uplifting on the edge of the MAR. The shear zone along the detachment surface is
568 characterized by heterogeneous, variably altered and deformed gabbroic and peridotite lithologies
569 with extensive silica metasomatism. Fluids were focused along the detachment and discrete ductile
570 shear zones triggering metasomatism of serpentinites and gabbros, resulting in talc-amphibole-
571 chlorite schist lenses. The footwall shows widespread, ongoing serpentinization related to a
572 complex network of steeply dipping faults that enhance infiltration of seawater into the fresh
573 peridotite promoting the development of pervasive to localize serpentinization and propagation of
574 the serpentinization front, which ultimately lead to the formation of the LCHF. Black squares

575 indicate hypothetical locations within the oceanic core complex of carbonate formation during
576 different stages in the hydrothermal evolution of the Atlantis Massif and are detailed in Figure 10.

577

578 Calcite IIa is not only characterized by higher MgO but also by higher FeO contents (Figure
579 7a). We suggest that high temperatures and higher fluid fluxes may result in elevated Fe^{2+}
580 concentrations in the fluid and consequently in the calcites. McCollom and Bach (2009) showed
581 that high temperatures (T = 100°C) and high water/rock ratios (W:R > 2) result in lower
582 concentrations of Fe in the secondary minerals brucite and serpentine, leading to the formation of
583 a higher amount of magnetite and H_2 (see also Malvoisin, 2015). This may also result in higher
584 Fe^{2+} concentration in solution. In fact, at the Atlantis Massif, higher magnetite concentrations (5
585 to 8 vol%) are observed at sites influenced by mafic intrusions. In addition, higher amounts of
586 magnetite have been associated with more oxidizing conditions caused by higher fluid flow
587 (Andreani et al., 2009; Ulrich et al., 2014) supporting the argument of higher water/rock ratios and
588 influx of seawater. High alteration temperatures and increased mixing of fresh seawater in the
589 hydrothermal fluid is also supported by clumped isotope investigations of the same samples
590 ($\delta^{13}C_{cc\ I}$ = -2.7 ‰, $T_{\Delta47}$ = 145 to 185°C; $\delta^{13}C_{cc\ II}$ = -0.7 ‰, $T_{\Delta47}$ = 145°C). Calcite II in olivine
591 cores occurs either dispersed in the rocks or is associated with calcite II veins. The similarity of
592 the element patterns suggests that replacive calcite II formed simultaneously from a similar
593 hydrothermal fluid as calcite II in the veins.

594 5.1.2 Magnesite and dolomite formation within oceanic peridotites

595 Hole M0076B consists mainly of peridotites and exhibits the highest diversity of carbonate
596 phases, including magnesite, dolomite, calcite and aragonite. The ultramafic rocks of this hole
597 show no evidence of silica metasomatism and thus provide constraints on carbonate formation in
598 the absence of mafic intrusions (Figure 10, frame 4 - 6). The first generation of carbonate is either
599 magnesite or dolomite forming syn- to post- serpentinization in veins and/or replacing serpentine
600 and olivine (Figure 10.5). Dolomite, and especially magnesite precipitation, requires high Mg/Ca
601 ratios in the fluids (e.g., Hövelmann et al., 2011; Lumsden et al., 1995; Peuble, Godard, et al.,
602 2015). Thermodynamic studies predict that magnesite should form during the reaction of
603 serpentinite and CO_2-bearing aqueous fluids (e.g., Grozeva et al., 2017; Klein & Garrido, 2011).

However, only a few studies have reported magnesite in oceanic serpentinites (Gablina et al., 2006) whereas it is more common in altered ultramafic rocks on land (soapstone and listvenite). Previous studies suggest that magnesite in oceanic settings may form in Ca-poor ultramafic rocks, such as dunite or completely serpentinized peridotite, or where a sustained influx of CO_2-rich fluids leads to silica activities in the fluid ($a SiO_{2(aq)}$) exceeding the stability of serpentine and consequently leading to high Mg/Ca ratios in the fluid (Figure 8a) (Barnes & O'Neil, 1969; Grozeva et al., 2017; Klein & Garrido, 2011). However, magnesite veins at the Atlantis Massif are found in highly serpentinized harzburgites with no evidence for serpentine instability. Indeed thermodynamic studies predict that relatively low $a SiO_{2(aq)}$, imposed by serpentine and brucite formation and lower dissolution rates of the primary minerals, leads to stabilization of clinopyroxene and thus to lower $Ca^{2+}_{(aq)}$ in the fluids (Figure 8a) (e.g., Klein et al., 2013). Based on thermodynamic models (Grozeva et al., 2017), we argue that high $CO_{2(aq)}$ and moderate $SiO_{2(aq)}$ concentrations in the hydrothermal fluid has led to serpentinization of orthopyroxene and olivine, while preserving clinopyroxene, which should have been sufficient to maintain high Mg/Ca ratios and favour the precipitation of Mg-rich carbonates (Figure 8b).

Magnesite is absent in most samples, even though high MgO content in calcites indicates high Mg^{2+} in solution. This suggests that $CO_{2(aq)}$ concentration alone does not control magnesite precipitation at the Atlantis Massif. An additional factor, such as confined flow pathways with limited fluid fluxes may be necessary for magnesite formation. Pokrovsky & Schott (2002) and Schott et al. (2009) showed that a high fluid flux kinetically favours the formation of Ca-rich rather than Mg-rich carbonates, due to different properties of Mg^{2+} and Ca^{2+} ions. The limiting step for carbonate crystallization is the dehydration of cations at the crystal surface. The lower the rate of water molecule exchange in the first hydration sphere of a metal ion, the lower the crystallization rate of a metal carbonate. Studies showed that the rate of water molecule exchange from the fluid into the cation hydration sphere is faster for Ca^{2+} than Mg^{2+} (e.g., Pokrovsky & Schott, 2002), which explains the different precipitation rates of Ca-rich (fast) and Mg-rich (slow) carbonates. Thus, dolomite will precipitate under conditions of moderate fluid fluxes when the fluid contains Ca even in a Mg-rich system, and magnesite will precipitate in rock-dominated systems in zones of more-reduced fluid flow (Peuble, Andreani, et al., 2015). Dolomite replacing serpentine or olivine occurs either dispersed in the rocks or is associated with dolomite veins. The similarity of

634 the element patterns suggests that replacive dolomite formed at the same time from a similar
635 hydrothermal fluid as dolomite in the veins.

636 The formation of magnesite and dolomite is followed by precipitation of calcite II at Hole
637 M0076B (Figure 10.6). The continuous hydration of the basement can lead to an increase of the
638 activity of SiO_2, which would lead to a dissolution of clinopyroxene (Figure 8a) and consequently
639 to a lower Mg/Ca ratios in the fluids favouring calcite formation. In addition, a potential higher
640 influx of seawater caused by the progressive uplift of the massif may also result in an increase in
641 fluid fluxes through brittle deformation, which favours the formation of Ca-rich carbonates (see
642 magnesite discussion). Both calcite II (calcite IIa, calcite IIb) subgroups are observed (Figure 7b
643 and d), indicating that high Mg^{2+} concentrations are maintained as the system evolves. The
644 compositional variability of the hydrothermal fluids can be caused by changes in precipitation
645 and/or dissolution rates, in the influx of fresh seawater and changing temperatures. The high
646 variability is also observed in the variable and high FeO and MnO contents of calcite II; whereby,
647 a systematic difference between the subgroups cannot be observed.

648 The last carbonate phases are calcite III and aragonite precipitating in veins (Figure 10.6):
649 They have low FeO contents, which points to precipitation in equilibrium with cold hydrothermal
650 fluids and mixing with unaltered seawater. In some cases, the botryoidal texture of calcite III
651 (Figure 4d - e; Figure 6) indicates precipitation from a percolating solution within an open space.
652 These spaces are often fractures crosscutting all minerals and deformation textures of the
653 ultramafic rock, indicating that they formed after tectonic deformation of the serpentinite (Klein
654 et al., 2015). Precipitation from cold, unaltered seawater mixing with evolved hydrothermal fluid
655 is confirmed by clumped isotope temperatures of calcite III of $T_{\Delta 47}$ = 1 to 8°C ($\delta^{18}O_{cc\ III}$ = ~ 4.0
656 ‰ VPDB) and seawater like carbon isotopes $\delta^{13}C_{cc\ III}$ = +1.7 to +2.2 ‰, and for aragonite by $T_{\Delta 47,\ arg}$ = 1 to 4°C ($\delta^{18}O_{arg}$ = ~ 3.9 ‰ VPDB), and a $\delta^{13}C_{arg}$ = -1.5 to -0.1 ‰. This range also matches
658 the isotopic composition of the carbonate chimneys from the LCHF that are caused by mixing of
659 the venting fluid with the surrounding seawater, and show $\delta^{13}C$ values close to marine values
660 within 2 per mil of 0 ‰ for most of the samples and $\delta^{18}O$ values >2 ‰ VPDB (Kelley et al., 2005),
661 which is consistent with late precipitation of calcite III and aragonite.

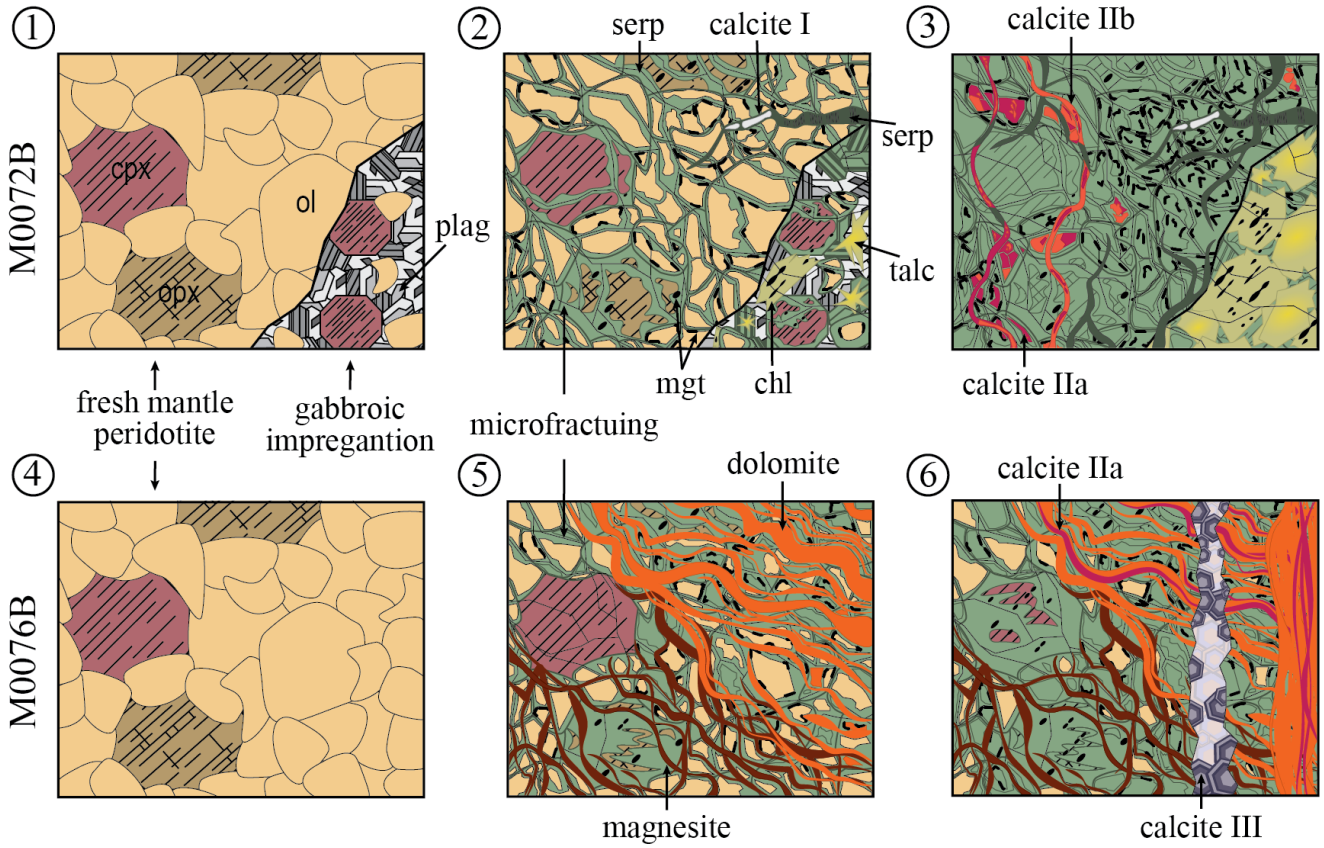

Figure 10. Conceptual model for the development of alteration heterogeneities in domains of the footwall along the detachment fault plane at the Atlantis Massif illustrating (1 to 3) alteration characteristics of Hole M0072B and (4 to 6) representative alteration textures of Hole M0076B. The combination of anisotropic thermal contraction and tectonic stresses in the brittle domain of the mantle leads to pervasive micro-fracturing (Rouméjon et al., 2014), providing a fine network of pathways for serpentinization and carbonate precipitation. Hypothetical location of the illustrated lithologies can be seen in Figure 9. Hole M0072B is characterized by fully serpentinized peridotites with high magnetite concentration and carbonate precipitation in proximity to significant silica metasomatism of gabbroic and peridotite lithologies. The alteration of gabbroic lithologies provides a higher concentration of Ca in the hydrothermal fluid and leads to calcite I, IIa and IIb formation. Calcite I represents carbonate formation during early hydration, whereas calcite IIa and IIb represent later formation. Carbonate precipitation at Hole M0076B is controlled by a high Mg/Ca ratio and zones of reduced flow due to structural heterogeneities, which leads to

676 the early formation of magnesite and dolomite along microfractures. As exhumation and
677 serpentinization proceeds, alteration of clinopyroxene provides enough Ca for calcite IIa formation
678 and less altered seawater leads later to calcite III precipitation inside fractures. See text for a
679 detailed discussion.

680

681 5.1.3 Carbonate formation at the periphery of the hydrothermal system

682 Peridotites at Hole M0069A are covered by ~7 m of sediments and dolerites but do not
683 show evidence for silica metasomatism. Rouméjon, Früh-Green, et al. (2018) showed that the
684 basement at this site is characterized by pervasive serpentinization without late overprinting and
685 recrystallization. Thus, this site provides information on the alteration at the periphery of an active
686 hydrothermal system with low degrees of fluid-rock interactions.

687 Carbonate is only present in aragonite veins, which are the volumetrically dominant
688 carbonate phase at the AM. Geochemical and textural features are comparable to aragonite from
689 sites in the vicinity of the hydrothermal system. Aragonite formed at low temperatures ($T_{\Delta47,\,arg}$ =
690 1 to 7°C) from fairly unmodified seawater ($\delta^{13}C_{arg}$ = -0.2 to 1.6 ‰). At such conditions, aragonite
691 precipitation is favoured over calcite due to high Mg^{2+} and sulfate concentrations (Burton, 1993;
692 Eickmann, Bach, & Peckmann, 2009). The lack of carbonate veins within the dolerite, and the
693 relative high vein density in the peridotites below it, strengthens previous interpretations that
694 dolerite domains constitute impermeable barriers and fluids are channelled along the walls of the
695 intrusion (Rouméjon & Cannat, 2014).

696 5.2 Manganese concentration in carbonates from the Atlantis Massif

697 Carbonates are in general a favourable sink for Mn (Deer et al., 1992) and hydrothermal
698 systems are important sources of manganese (e.g., Charlou et al., 2002; Klinkhammer et al., 1977).
699 Laboratory studies have shown that seawater tends to leach manganese from mid-ocean ridge
700 basalts at elevated temperatures (T > 200°C) and pressures (P > 500 bar), causing an increase of
701 Mn^{2+} in solution (Bischoff & Dickson, 1975; Mottl et al., 1979). Previous studies of calcite
702 cements formed in shallow fresh-water aquifers provide evidence that the uptake of Mn^{2+} in
703 carbonates is mainly dependent on Eh which controls Mn solubility (Barnaby & Rimstidt, 1989;
704 Dromgoole & Walter, 1990). Most marine low-temperature carbonates have MnO contents of ~1

wt% (e.g., Eickmann, Bach, Rosner, et al., 2009; Picazo et al., 2020). At the Atlantis Massif, carbonates exhibit remarkably high and variable MnO concentrations, and we argue that this is caused by a change in the redox state of the hydrothermal fluid. The high MnO contents would indicate a low redox state, typical of serpentinizing environments, and a shift to lower MnO would indicate a progressive increase in Eh. Most carbonate veins at the AM do not show a systematic change with their sequence of precipitation except for a thicker dolomite vein. In this vein, early dolomites have higher MnO ($MnO_{max, dol}$ = 6 wt%) than younger generations (Figure 6b), which may indicate a change to higher oxygen fugacity of the fluid over time. This change in fluid composition is also indicated by dissolved surfaces and pitted textures in early dolomites (Figure 3i).

At the Mid-Atlantic Ridge, carbonates with extremely high MnO contents (max. 9.5 wt% Mn; Schroeder et al., 2015) have been previously reported. Carbonates from ODP Site 1275 (35 km north of the 15°20' Fracture Zone and 30 km west of the MAR axis) have high MnO contents and were correlated to an early, high-temperature (T_{max} = 174°C) stage of formation. These carbonate veins occur within gabbros and troctolites, which most likely were the source of the elevated Mn. At the AM, carbonates are less common in the mafic rocks and contain MnO contents below 0.1 wt%. However, we do observe higher MnO ($MnO_{max, M0072B}$ = 7.3 wt%) in carbonates in proximity to mafic intrusions, compared to carbonates that formed in the periphery to mafic intrusions. We propose that the high MnO concentrations are consistent with highly reducing serpentinizing fluids at the AM, leaching high amounts of Mn^{2+} from the interlayered gabbroic bodies, and transport to domains where cooling of hydrothermal fluids and or mixing with seawater leads to the formation of carbonates.

5.3 Carbonates as a CO_2 sink within the oceanic lithosphere

Recently, carbonate formation in ultramafic rocks has received considerable attention as a means to sequester atmospheric CO_2 (e.g., Kelemen & Matter, 2008), and studies of various ophicalcites showed that carbon is stored over millions of years (Bachu et al., 1994; Kelemen et al., 2011; Schwarzenbach, Früh-Green, et al., 2013; Seifritz, 1990). Studies of modern and ancient serpentinites estimate that up to 10 wt% total inorganic carbon is fixed as carbonates during serpentinization and carbonate precipitation, and that approximately 10% of all carbon that is cycled through the ocean is incorporated into the oceanic lithosphere during alteration of oceanic

735 crust (Alt et al., 2013; Schwarzenbach, Früh-Green, et al., 2013). To better evaluate the potential
736 of ultramafic rocks as long term storage for CO_2, quantitative information on the sources and sinks
737 of carbon is necessary. One critical factor contributing to the continuing uncertainty on this topic
738 is the difficulty in obtaining samples directly from subsurface environments near mid-ocean ridges
739 for analysis of carbon compounds, and most estimations are based on information inferred from
740 analysis of hydrothermal fluids discharged at the seafloor. Most of these hydrothermal vents have
741 CO_2 concentrations that are substantially higher than the amount of dissolved inorganic carbon
742 (DIC: $CO_{2(aq)} + HCO_3^- + CO_3^{2-}$) in seawater. However, ^{13}C and ^{14}C isotope analyses of CO_2 in
743 hydrothermal fluids from the Endeavour system (high temperature basaltic dominated
744 hydrothermal system) indicates that most of the seawater DIC is removed from circulating fluids
745 and stored as carbonates within the basement before discharge at hydrothermal vents on the
746 seafloor (Proskurowski et al., 2004). It is assumed that this is true for most hydrothermal systems
747 (McCollom, 2008; and references therein).

748 In contrast to basalt-hosted hydrothermal systems, the vent fluids from the Lost City
749 hydrothermal system are highly depleted in DIC (Proskurowski et al., 2008), which leads to the
750 assumption that the AM should contain significant carbonate deposits. Thus, one of the main goals
751 of IODP Expedition 357 was to investigate the distribution of carbonate deposits within the
752 basement of the Atlantis Massif. Our results show that the amount of inorganic carbon in the
753 shallow basement holes is relatively low. Carbonates are almost exclusively observed close to the
754 active venting LCHF and rarely at other locations along the southern wall. The distribution of
755 carbonates throughout the cores from the central Sites (M0069, M0072, M0076) is heterogeneous
756 with an overall carbonate vein abundance estimated at ~2 vol%. However, because the maximum
757 depth reached was 16.4 mbsf, we do not know how high the concentrations are at depth. We
758 propose that most of the DIC removal occurred during deeper circulation of the fluid and that
759 shallow parts of the AM record carbonate precipitation associated with present-day hydrothermal
760 circulation and driven by localized shallow fluid circulation along fractures.

761 Additionally, the AM is a relatively young exhumed mantle sequence, and our study
762 provides evidence that CO_2 uptake by low-temperature aragonite formation is, in general, low at
763 young serpentinized mantle, but may increase if fracturing and veining continue for tens of
764 millions of years. A low abundance of low-temperature aragonite veins in young serpentinized
765 mantle is also observed at ODP Site 895 at Hess Deep (Blusztajn & Hart, 1996), ODP Site 920

766 south of the Kane Fracture Zone (Alt & Shanks, 1998) and from ODP Site 175 at the Mid-Atlantic
767 Ridge (Schroeder et al., 2015). The data presented here provide information on the fate of carbon
768 in the oceanic lithosphere and will help to better evaluate whether hydration and serpentinization
769 of oceanic crust is a globally significant sink for CO_2. Further investigations of deeper drill holes
770 and older oceanic core complexes would be necessary.

771 **6 Conclusions**

772 We investigated the alteration of peridotites in seven drill holes at five sites across the
773 southern wall of the Atlantis Massif recovered during IODP Expedition 357. We developed a
774 conceptual model for the genesis of carbonates in oceanic lithosphere. Detailed textural,
775 mineralogical and geochemical investigations reveal variable alteration between holes that
776 represent different portions of the footwall exhumed in the vicinity of the detachment fault zone.
777 Three characteristic types of carbonate occurrences, including the minerals magnesite, dolomite,
778 calcite and aragonite, could be identified. All occurrences formed close to the actively venting
779 LCHF under different conditions and were controlled by (i) fluid composition and flow, (ii)
780 temperature, and (iii) influence of mafic intrusions. $SiO_{2(aq)}$, $CO_{2(aq)}$ and Mg^{2+} concentrations of
781 the hydrothermal fluid have particularly significant impacts on the carbonate compositions.

782 Even though carbonates within this oceanic hydrothermal system indicate ubiquitous high
783 Mg^{2+} concentrations, only limited amounts of magnesite and/or dolomite, are formed, suggesting
784 that kinetic factors impede the formation of Mg-bearing carbonates relative to Ca-carbonates. This
785 supports the hypothesis that both a high Mg/Ca ratio and confined flow are necessary to precipitate
786 Mg-carbonates. In addition, our study indicate that lower Mg^{2+} concentrations in solution
787 characterize hydrothermal fluids in proximity to mafic intrusions. This lower Mg^{2+} in solution in
788 proximity to mafic intrusions in combination with the necessary lower fluid flow may limit
789 magnesite formation in the oceanic lithosphere, since we know that hydrothermal systems at mid-
790 ocean ridges often contain mafic intrusions and are, in general, characterized by high fluid flow
791 (Bach et al., 2011). Therefore, the formation of magnesite in oceanic settings is likely limited to
792 domains of ultramafic rocks without major mafic intrusions and less rapid upflow of hydrothermal
793 fluids.

794 Our study shows that Ca-Mg carbonates, as a significant part of the process of hydration
795 and alteration of oceanic peridotites, represent an important tool to reconstruct alteration histories

of serpentinized peridotites. Moreover, Ca-Mg carbonates may represent a significant sink of carbon from the seawater and or the mantle that would otherwise reenter/enter the oceans. Thus, carbonate-containing oceanic serpentinite transported into subduction zones may represent an additional carbon reservoir recycled into the deep mantle. Age determinations show that shallow carbonates formed over a narrow time interval from 37,000 to 23,000 yr, corresponding to the early stages of the Lost City hydrothermal system (Früh-Green et al., 2003). The active vents at Lost City still show highly depleted DIC contents, which suggests that carbonate is continuing to be formed at deeper levels of this off-axis hydrothermal system.

The results of our study are of interest not only for the investigation of ancient and present-day carbonation systems, but they may also be of interest for the interpretation of artificial carbonation of serpentinite on land, at the seafloor or in laboratory experiments. We show that thermodynamically predicted magnesite precipitation occurs locally within oceanic serpentinized and highlights the high heterogeneity of hydrothermal fluids circulating within the footwall exhumed at the Atlantis Massif, and probably in any detachment system.

Acknowledgements

We would like to thank Madalina Jaggi, Julien Allaz, Lydia Zehnder and Andreas Jallas for help with sample preparation and analyses as well as the European Consortium for Ocean Research Drilling (ECORD) and the IODP Expedition 357 science party for providing drill core samples for this study. We gratefully acknowledge funding by the Swiss National Science Foundation (SNF) project No. 200021_163187 to Früh-Green. Results of individual analyses of the samples will be available online on PANGAEA (www.pangaea.de).

References

Allen, D. E., & Seyfried, W. E. (2003). Compositional controls on vent fluids from ultramafic-hosted hydrothermal systems at mid-ocean ridges: An experimental study at 400°C, 500 bars. *Geochimica et Cosmochimica Acta*, *67*(8), 1531–1542. https://doi.org/10.1016/S0016-7037(02)01173-0

Alt, J. C., & Shanks, W. C. (1998). Sulfur in serpentinized oceanic peridotites: Serpentinization processes and microbial sulfate reduction. *Journal of Geophysical Research: Solid Earth*, *103*(B5), 9917–9929. https://doi.org/10.1029/98jb00576

Alt, J. C., Schwarzenbach, E. M., Früh-Green, G. L., Shanks, W. C., Bernasconi, S. M., Garrido, C. J., et al. (2013). The role of serpentinites in cycling of carbon and sulfur: Seafloor serpentinization and subduction metamorphism. *Lithos*, *178*, 40–54. https://doi.org/10.1016/j.lithos.2012.12.006

Andreani, M., Luquot, L., Gouze, P., Godard, M., Hoisé, E., & Gibert, B. (2009). Experimental Study of Carbon Sequestration Reactions Controlled by the Percolation of CO 2 -Rich Brine through Peridotites. *Environmental Science & Technology*, *43*(4), 1226–1231. https://doi.org/10.1021/es8018429

Bach, W., Garrido, C. J., Paulick, H., Harvey, J., & Rosner, M. (2004). Seawater-peridotite interactions: First insights from ODP Leg 209, MAR 15°N. *Geochemistry, Geophysics, Geosystems*, *5*(9). https://doi.org/10.1029/2004GC000744

Bach, W., Rosner, M., Jöns, N., Rausch, S., Robinson, L. F., Paulick, H., & Erzinger, J. (2011). Carbonate veins trace seawater circulation during exhumation and uplift of mantle rock: Results from ODP Leg 209. *Earth and Planetary Science Letters*, *311*(3–4), 242–252. https://doi.org/10.1016/j.epsl.2011.09.021

Bachu, S., Gunter, W. D., & Perkins, E. H. (1994). Aquifer disposal of CO2: Hydrodynamic and mineral trapping. *Energy Conversion and Management*, *35*(4), 269–279. https://doi.org/10.1016/0196-8904(94)90060-4

Barnaby, R. J., & Rimstidt, J. D. (1989). Redox conditions of calcite cementation interpreted from Mn and Fe contents of authigenic calcites. *Geological Society of America Bulletin*, *101*(6), 795–804. https://doi.org/10.1130/0016-7606(1989)101<0795:RCOCCI>2.3.CO;2

Barnes, I., & O'Neil, J. R. (1969). The relationship between fluids in some fresh alpine-type ultramafics and possible modern serpentinization, western United States. *Bulletin of the Geological Society of America*, *80*(10), 1947–1960. https://doi.org/10.1130/0016-7606(1969)80[1947:TRBFIS]2.0.CO;2

Barnes, I., O'Neil, J. R., Rapp, J. B., & White, D. E. (1973). Silica-carbonate alteration of serpentine: Wall rock alteration in mercury deposits of the California Coast Ranges. *Economic Geology*, *68*(3), 388–398. https://doi.org/10.2113/gsecongeo.68.3.388

Beinlich, A., Plümper, O., Hövelmann, J., Austrheim, H., & Jamtveit, B. (2012). Massive serpentinite carbonation at Linnajavri, N-Norway. *Terra Nova*, *24*(6), 446–455. https://doi.org/10.1111/j.1365-3121.2012.01083.x

Berndt, M. E., Seyfried, W. E., & Janecky, D. R. (1989). Plagioclase and epidote buffering of cation ratios in mid-ocean ridge hydrothermal fluids: Experimental results in and near the

supercritical region. *Geochimica et Cosmochimica Acta*, *53*(9), 2283–2300. https://doi.org/10.1016/0016-7037(89)90351-7

Bischoff, J. L., & Dickson, F. W. (1975). Seawater-basalt interaction at 200°C and 500 bars: Implications for origin of sea-floor heavy-metal deposits and regulation of seawater chemistry. *Earth and Planetary Science Letters*, *25*(3), 385–397. https://doi.org/10.1016/0012-821X(75)90257-5

Blackman, D. K., Cann, J. R., Janssen, B., & Smith, D. K. (1998). Origin of extensional core complexes: Evidence from the Mid-Atlantic Ridge at Atlantis Fracture Zone. *Journal of Geophysical Research: Solid Earth*, *103*(B9), 21315–21333. https://doi.org/10.1029/98jb01756

Blackman, D. K., Karson, J. A., Kelley, D. S., Cann, J. R., Früh-Green, G. L., Gee, J. S., et al. (2002). Geology of the Atlantis Massif (Mid-Atlantic Ridge, 30° N): Implications for the evolution of an ultramafic oceanic core complex. *Marine Geophysical Researches*, *23*(5/6), 443–469. https://doi.org/10.1023/B:MARI.0000018232.14085.75

Blusztajn, J. S., & Hart, S. R. (1996). Sr and O Isotopic Ratios of Aragonite Veins from Site 895. *Proceedings of the Ocean Drilling Program, 147 Scientific Results*, *147*, 311–313. https://doi.org/10.2973/odp.proc.sr.147.035.1996

Bohlke, J. K. (1989). Comparison of metasomatic reactions between a common CO2-rich vein fluid and diverse wall rocks: intensive variables, mass transfers, and Au mineralization at Alleghany, California. *Economic Geology*, *84*(2), 291–327. https://doi.org/10.2113/gsecongeo.84.2.291

Bonatti, E., Emiliani, C., Ferrara, G., Honnorez, J., & Rydell, H. (1974). Ultramafic-carbonate breccias from the equatorial Mid Atlantic Ridge. *Marine Geology*, *16*(2), 83–102. https://doi.org/10.1016/0025-3227(74)90057-7

Bonatti, E., Lawrence, J. R., Hamlyn, P. R., & Breger, D. (1980). Aragonite from deep sea ultramafic rocks. *Geochimica et Cosmochimica Acta*, *44*(8), 1207–1214. https://doi.org/10.1016/0016-7037(80)90074-5

Boschi, C., Früh-Green, G. L., Delacour, A., Karson, J. A., & Kelley, D. S. (2006). Mass transfer and fluid flow during detachment faulting and development of an oceanic core complex, Atlantis Massif (MAR 30°N). *Geochemistry, Geophysics, Geosystems*, *7*(1). https://doi.org/10.1029/2005GC001074

Boschi, C., Dini, A., Früh-Green, G. L., & Kelley, D. S. (2008). Isotopic and element exchange during serpentinization and metasomatism at the Atlantis Massif (MAR 30°N): Insights from B and Sr isotope data. *Geochimica et Cosmochimica Acta*, *72*(7), 1801–1823. https://doi.org/10.1016/j.gca.2008.01.013

Boschi, C., Dini, A., Dallai, L., Ruggieri, G., & Gianelli, G. (2009). Enhanced CO2-mineral sequestration by cyclic hydraulic fracturing and Si-rich fluid infiltration into serpentinites at Malentrata (Tuscany, Italy). *Chemical Geology*, *265*(1–2), 209–226. https://doi.org/10.1016/j.chemgeo.2009.03.016

Bruni, J., Canepa, M., Chiodini, G., Cioni, R., Cipolli, F., Longinelli, A., et al. (2002). Irreversible water-rock mass transfer accompanying the generation of the neutral, Mg–

HCO3 and high-pH, Ca–OH spring waters of the Genova province, Italy. *Applied Geochemistry*, *17*(4), 455–474. https://doi.org/10.1016/S0883-2927(01)00113-5

Burton, E. A. (1993). Controls on marine carbonate cement mineralogy: review and reassessment. *Chemical Geology*, *105*(1–3), 163–179. https://doi.org/10.1016/0009-2541(93)90124-2

Cann, J. R., Blackman, D. K., Smith, D. K., McAllister, E., Janssen, B., Mello, S., et al. (1997). Corrugated slip surfaces formed at ridge–transform intersections on the Mid-Atlantic Ridge. *Nature*, *385*(6614), 329–332. https://doi.org/10.1038/385329a0

Cannat, M., Fontaine, F., & Escartín, J. (2010). Serpentinization and associated hydrogen and methane fluxes at slow-spreading ridges. In *Diversity of Hydrothermal Systems on Slow Spreading Ocean Ridges* (pp. 241–264). https://doi.org/10.1029/2008GM000760

Carlson, R. L. (2001). The abundance of ultramafic rocks in Atlantic Ocean crust. *Geophysical Journal*, *144*(1), 37–48.

Charlou, J. L., Donval, J. P., Fouquet, Y., Jean-Baptiste, P., & Holm, N. G. (2002). Geochemistry of high H2 and CH4 vent fluids issuing from ultramafic rocks at the Rainbow hydrothermal field (36°14′N, MAR). *Chemical Geology*, *191*(4), 345–359. https://doi.org/10.1016/S0009-2541(02)00134-1

Cipolli, F., Gambardella, B., Marini, L., Ottonello, G., & Zuccolini, M. V. (2004). Geochemistry of high-pH waters from serpentinites of the Gruppo di Voltri (Genova, Italy) and reaction path modeling of CO2 sequestration in serpentinite aquifers. *Applied Geochemistry*, *19*(5), 787–802. https://doi.org/10.1016/j.apgeochem.2003.10.007

Dabitzias, S. G. (1980). Petrology and Genesis of the Vavdos Cryptocrystalline Magnesite Deposits, Chalkidiki Peninsula, Northern Greece. *Economic Geology*, *75*(8), 1138–1151. https://doi.org/10.2113/gsecongeo.75.8.1138

Von Damm, K. L., Bray, A. M., Buttermore, L. G., & Oosting, S. E. (1998). The geochemical controls on vent fluids from the Lucky Strike vent field, Mid-Atlantic Ridge. *Earth and Planetary Science Letters*, *160*(3–4), 521–536. https://doi.org/10.1016/S0012-821X(98)00108-3

Deer, W. A., Howie, R. A., & Zussman, J. (1992). *Introduction to the Rock-Forming Minerals* (2nd ed.). London: Longman.

Detrick, R. S., & Collins, J. A. (1998). Seismic structure of ultramafics exposed at shallow crustal levels in the Mid-Atlantic Ridge rift valley at 15°N. *Eos Trans. AGU*, *79*(45), Fall Meet. Suppl., F800.

Donovan, J. J., & Tingle, T. N. (1996). An Improved Mean Atomic Number Background Correction for Quantitative Microanalysis. *Microscopy and Microanalysis*, *2*(1), 1–7. https://doi.org/10.1017/S1431927696210013

Donovan, J. J., Singer, J. W., & Armstrong, J. T. (2016). A new EPMA method for fast trace element analysis in simple matrices. *American Mineralogist*, *101*(8), 1839–1853. https://doi.org/10.2138/am-2016-5628

Douville, E., Charlou, J. L., Oelkers, E. H., Bienvenu, P., Jove Colon, C. ., Donval, J. P., et al. (2002). The rainbow vent fluids (36°14′N, MAR): the influence of ultramafic rocks and

940 phase separation on trace metal content in Mid-Atlantic Ridge hydrothermal fluids.
941 *Chemical Geology*, *184*(1–2), 37–48. https://doi.org/10.1016/S0009-2541(01)00351-5

942 Dromgoole, E. L., & Walter, L. M. (1990). Iron and manganese incorporation into calcite:
943 Effects of growth kinetics, temperature and solution chemistry. *Chemical Geology*, *81*(4),
944 311–336. https://doi.org/10.1016/0009-2541(90)90053-A

945 Eickmann, B., Bach, W., & Peckmann, J. (2009). Authigenesis of carbonate minerals in modern
946 and Devonian ocean-floor hard rocks. *Journal of Geology*, *117*(3), 307–323.
947 https://doi.org/10.1086/597362

948 Eickmann, B., Bach, W., Rosner, M., & Peckmann, J. (2009). Geochemical constraints on the
949 modes of carbonate precipitation in peridotites from the Logatchev Hydrothermal Vent
950 Field and Gakkel Ridge. *Chemical Geology*, *268*(1–2), 97–106.
951 https://doi.org/10.1016/j.chemgeo.2009.08.002

952 Falk, E. S., & Kelemen, P. B. (2015). Geochemistry and petrology of listvenite in the Samail
953 ophiolite, Sultanate of Oman: Complete carbonation of peridotite during ophiolite
954 emplacement. *Geochimica et Cosmochimica Acta*, *160*, 70–90.
955 https://doi.org/10.1016/j.gca.2015.03.014

956 Frost, R. B. (1985). On the stability of sulfides, oxides, and native metals in serpentinite. *Journal*
957 *of Petrology*, *26*(1), 31–63. https://doi.org/10.1093/petrology/26.1.31

958 Frost, R. B., & Beard, J. S. (2007). On silica activity and serpentinization. *Journal of Petrology*,
959 *48*(7), 1351–1368. https://doi.org/10.1093/petrology/egm021

960 Früh-Green, G. L., Kelley, D. S., Bernasconi, S. M., Karson, J. A., Ludwig, K. A., Butterfield, D.
961 A., et al. (2003). 30,000 Years of Hydrothermal Activity at the Lost City Vent Field.
962 *Science*, *301*(5632), 495–498. https://doi.org/10.1126/science.1085582

963 Früh-Green, G. L., Connolly, J. A. D., Plas, A., Kelley, D. S., & Grobéty, B. (2004).
964 Serpentinization of oceanic peridotites: Implications for geochemical cycles and
965 biological activity. In *The Subseafloor Biosphere at Mid-Ocean Ridges* (pp. 119–136).
966 https://doi.org/10.1029/144GM08

967 Früh-Green, G. L., Orcutt, B. N., Green, S. L., Cotterill, C., Morgan, S., Akizawa, N., et al.
968 (2017). Expedition 357 summary. *Proceedings of the International Ocean Discovery*
969 *Program*, *357*. https://doi.org/10.14379/iodp.proc.357.101.2017

970 Früh-Green, G. L., Orcutt, B. N., Rouméjon, S., Lilley, M. D., Morono, Y., Cotterill, C., et al.
971 (2018). Magmatism, serpentinization and life: Insights through drilling the Atlantis
972 Massif (IODP Expedition 357). *Lithos*, *323*, 137–155.
973 https://doi.org/10.1016/j.lithos.2018.09.012

974 Gablina, I. F., Semkova, T. A., Stepanova, T. V., & Gor'kova, N. V. (2006). Diagenetic
975 alterations of copper sulfides in modern ore-bearing sediments of the Logatchev-1
976 hydrothermal field (Mid-Atlantic Ridge 14°45′ N). *Lithology and Mineral Resources*,
977 *41*(1), 27–44. https://doi.org/10.1134/S0024490206010032

978 Gamo, T., Chiba, H., Yamanaka, T., Okudaira, T., Hashimoto, J., Tsuchida, S., et al. (2001).
979 Chemical characteristics of newly discovered black smoker fluids and associated
980 hydrothermal plumes at the Rodriguez Triple Junction, Central Indian Ridge. *Earth and*

Planetary Science Letters, *193*(3–4), 371–379. https://doi.org/10.1016/S0012-821X(01)00511-8

German, C. R., & Von Damm, K. L. (2003). Hydrothermal Processes. In *Treatise on Geochemistry* (pp. 181–222). Cambridge: Cambridge University Press. https://doi.org/10.1017/CBO9781139084260.009

Giammar, D. E., Bruant, R. G., & Peters, C. A. (2005). Forsterite dissolution and magnesite precipitation at conditions relevant for deep saline aquifer storage and sequestration of carbon dioxide. *Chemical Geology*, *217*(3-4 SPEC. ISS.), 257–276. https://doi.org/10.1016/j.chemgeo.2004.12.013

Götze, J. (2012). Application of cathodoluminescence microscopy and spectroscopy in geosciences. *Microscopy and Microanalysis*, *18*(6), 1270–1284. https://doi.org/10.1017/S1431927612001122

Greenwood, J., H. (1967). Mineral equilibria in the system MgO-SiO_2-H_2O-CO_2. *Researches in Geochemistry*, 542–547. Retrieved from http://ci.nii.ac.jp/naid/10004121523/en/

Grozeva, N. G., Klein, F., Seewald, J. S., & Sylva, S. P. (2017). Experimental study of carbonate formation in oceanic peridotite. *Geochimica et Cosmochimica Acta*, *199*, 264–286. https://doi.org/10.1016/j.gca.2016.10.052

Hansen, L. D., Dipple, G. M., Gordon, T. M., & Kellett, D. A. (2005). Carbonated serpentinite (listwanite) at Atlin, British Columbia: A geological analogue to carbon dioxide sequestration. *Canadian Mineralogist*, *43*(1), 225–239. https://doi.org/10.2113/gscanmin.43.1.225

Hess, H. H. (1933). The Problem of Serpentinization and the Origin of certain Chrysotile Asbestos Talc and Soapstone Deposits. *Economic Geology*, *28*, 634–657.

Hövelmann, J., Austrheim, H., Beinlich, A., & Anne Munz, I. (2011). Experimental study of the carbonation of partially serpentinized and weathered peridotites. *Geochimica et Cosmochimica Acta*, *75*(22), 6760–6779. https://doi.org/10.1016/j.gca.2011.08.032

Johannes, W. (1967). Zur Bildung und Stabilität von Forsterit, Talk, Serpentin, Quarz und Magnesit im System Mg0-Si02-H20-C02. *Contributions to Mineralogy and Petrology*, *15*, 233–250.

Johannes, W. (1969). An experimental investigation of the system MgO-SiO2-H2O-CO2. *American Journal of Science*, *267*(9), 1083–1104. https://doi.org/10.2475/ajs.267.9.1083

Karson, J. A., Früh-Green, G. L., Kelley, D. S., Williams, E. A., Yoerger, D. R., & Jakuba, M. (2006). Detachment shear zone of the Atlantis Massif core complex, Mid-Atlantic Ridge, 30 °n. *Geochemistry, Geophysics, Geosystems*, *7*(6), n/a-n/a. https://doi.org/10.1029/2005GC001109

Kelemen, P. B., & Matter, J. M. (2008). In situ carbonation of peridotite for CO2 storage. *Proceedings of the National Academy of Sciences of the United States of America*, *105*(45), 17295–17300. https://doi.org/10.1073/pnas.0805794105

Kelemen, P. B., Matter, J. M., Streit, E. E., Rudge, J. F., Curry, W. B., & Blusztajn, J. S. (2011). Rates and Mechanisms of Mineral Carbonation in Peridotite: Natural Processes and

Recipes for Enhanced, in situ CO 2 Capture and Storage. *Annual Review of Earth and Planetary Sciences*, *39*(1), 545–576. https://doi.org/10.1146/annurev-earth-092010-152509

Kelley, D. S., & Früh-Green, G. L. (2001). Volatile lines of descent in submarine plutonic environments: Insights from stable isotope and fluid inclusion analyses. *Geochimica et Cosmochimica Acta*, *65*(19), 3325–3346. https://doi.org/10.1016/S0016-7037(01)00667-6

Kelley, D. S., Karson, J. A., Blackman, D. K., Früh-Green, G. L., Butterfield, D. A., Lilley, M. D., et al. (2001). An off-axis hydrothermal vent field near the Mid-Atlantic Ridge at 30 degrees N. *Nature*, *412*(6843), 145–9. https://doi.org/10.1038/35084000

Kelley, D. S., Karson, J. A., Früh-Green, G. L., Yoerger, D. R., Shank, T. M., Butterfield, D. A., et al. (2005). A Serpentinite-Hosted Ecosystem: The Lost City Hydrothermal Field. *Science*, *307*(5714), 1428–1434. https://doi.org/10.1126/science.1102556

King, H. E., Plümper, O., & Putnis, A. (2010). Effect of secondary phase formation on the carbonation of olivine. *Environmental Science and Technology*, *44*(16), 6503–6509. https://doi.org/10.1021/es9038193

Klein, F., & Garrido, C. J. (2011). Thermodynamic constraints on mineral carbonation of serpentinized peridotite. *Lithos*, *126*(3–4), 147–160. https://doi.org/10.1016/j.lithos.2011.07.020

Klein, F., & McCollom, T. M. (2013). From serpentinization to carbonation: New insights from a CO2 injection experiment. *Earth and Planetary Science Letters*, *379*, 137–145. https://doi.org/10.1016/j.epsl.2013.08.017

Klein, F., Bach, W., & McCollom, T. M. (2013). Compositional controls on hydrogen generation during serpentinization of ultramafic rocks. *Lithos*, *178*, 55–69. https://doi.org/10.1016/j.lithos.2013.03.008

Klein, F., Humphris, S. E., Guo, W., Schubotz, F., Schwarzenbach, E. M., Orsi, W. D., & Karl, D. M. (2015). Fluid mixing and the deep biosphere of a fossil Lost City-type hydrothermal system at the Iberia Margin. *Proceedings of the National Academy of Sciences of the United States of America*, *112*(39), 12036–12041. https://doi.org/10.1073/pnas.1504674112

Klinkhammer, G., Bender, M., & Weiss, R. F. (1977). Hydrothermal manganese in the Galapagos Rift. *Nature*, *269*(5626), 319–320. https://doi.org/10.1038/269319a0

Koons, P. O. (1981). A study of natural and experimental metasomatic assemblages in an ultramafic-quartzofeldspathic metasomatic system from the Haast schist, South Island, New Zealand. *Contributions to Mineralogy and Petrology*, *78*(2), 189–195. https://doi.org/10.1007/BF00373780

Korzhinskii, D. S. (1959). Physicochemical basis of the analysis of the paragenesis of minerals:(English translation], New York, Consultants Bureau. *Inc., 142p*.

Kourkoumelis, N. (2013). PowDLL, a reusable .NET component for interconverting powder diffraction data: Recent developments. In L. O'Neill (Ed.), *ICDD Annual Spring Meetings* (Vol. 28, pp. 137–48).

1063 Lafay, R., Montes-Hernandez, G., Janots, E., Chiriac, R., Findling, N., & Toche, F. (2014).
1064 Simultaneous precipitation of magnesite and lizardite from hydrothermal alteration of
1065 olivine under high-carbonate alkalinity. *Chemical Geology*, *368*, 63–75.
1066 https://doi.org/10.1016/j.chemgeo.2014.01.008

1067 Lafuente, B., Downs, R. T., Yang, H., & Stone, N. (2015). 1. The power of databases: The
1068 RRUFF project. In T. Armbruster & R. M. Danisi (Eds.), *Highlights in Mineralogical*
1069 *Crystallography* (pp. 1–30). Berlin, München, Boston: De Gruyter (O).
1070 https://doi.org/10.1515/9783110417104-003

1071 Lilley, M. D., Butterfield, D. A., Lupton, J. E., & Olson, E. J. (2003). Magmatic events can
1072 produce rapid changes in hydrothermal vent chemistry. *Nature*, *422*(6934), 878–881.
1073 https://doi.org/10.1038/nature01569

1074 Lister, C. R. B. (1972). On the thermal balance of a mid-ocean ridge. *Geophys. J. R. Astron.*
1075 *Soc.*, *26*, 515–535.

1076 Ludwig, K. A., Kelley, D. S., Butterfield, D. A., Nelson, B. K., & Früh-Green, G. L. (2006).
1077 Formation and evolution of carbonate chimneys at the Lost City Hydrothermal Field.
1078 *Geochimica et Cosmochimica Acta*, *70*(14), 3625–3645.
1079 https://doi.org/10.1016/j.gca.2006.04.016

1080 Ludwig, K. A., Shen, C.-C., Kelley, D. S., Cheng, H., & Edwards, R. L. (2011). U-Th
1081 systematics and 230 Th ages of carbonate chimneys at the Lost City Hydrothermal Field.
1082 *Geochimica et Cosmochimica Acta*, *75*(7), 1869–1888.
1083 https://doi.org/10.1016/j.gca.2011.01.008

1084 Lumsden, D. N., Morrison, J. W., & Lloyd, R. V. (1995). The Role of Iron and Mg / Ca Ratio in
1085 Dolomite Synthesis at 192° C. *The Journal of Geology*, *103*(1), 51–61.

1086 Machel, H. G. (1985). Cathodoluminescence in Calcite and Dolomite and its Chemical
1087 Interpretation. *Geoscience Canada*, *12*(4), 139–147.

1088 Malvoisin, B. (2015). Mass transfer in the oceanic lithosphere: Serpentinization is not
1089 isochemical. *Earth and Planetary Science Letters*, *430*, 75–85.
1090 https://doi.org/10.1016/j.epsl.2015.07.043

1091 McCollom, T. M. (2008). Observational, experimental, and theoretical constraints on carbon
1092 cycling in mid-ocean ridge hydrothermal systems. *Geophysical Monograph Series*, *178*,
1093 193–213. https://doi.org/10.1029/178GM10

1094 McCollom, T. M., & Bach, W. (2009). Thermodynamic constraints on hydrogen generation
1095 during serpentinization of ultramafic rocks. *Geochimica et Cosmochimica Acta*, *73*(3),
1096 856–875. https://doi.org/10.1016/j.gca.2008.10.032

1097 Mottl, M. J., Holland, H. D., & Corr, R. F. (1979). Chemical exchange during hydrothermal
1098 alteration of basalt by seawater-II. Experimental results for Fe, Mn, and sulfur species.
1099 *Geochimica et Cosmochimica Acta*, *43*(6), 869–884. https://doi.org/10.1016/0016-
1100 7037(79)90225-4

1101 Naldrett, A. J. (1966). Tale-carbonate alteration of some serpentinized ultramafic rocks south of
1102 Timmins, Ontario. *Journal of Petrology*, *7*(3), 489–499.
1103 https://doi.org/10.1093/petrology/7.3.489

Nooner, S. L., Sasagawa, G. S., Blackman, D. K., & Zumberge, M. A. (2003). Structure of oceanic core complexes: Constraints from seafloor gravity measurements made at the Atlantis Massif. *Geophysical Research Letters*, *30*(8), 8–11. https://doi.org/10.1029/2003GL017126

Van Noort, R., Spiers, C. J., Drury, M. R., & Kandianis, M. T. (2013). Peridotite dissolution and carbonation rates at fracture surfaces under conditions relevant for in situ mineralization of CO2. *Geochimica et Cosmochimica Acta*, *106*, 1–24. https://doi.org/10.1016/j.gca.2012.12.001

Paukert, A. N., Matter, J. M., Kelemen, P. B., Shock, E. L., & Havig, J. R. (2012). Reaction path modeling of enhanced in situ CO2 mineralization for carbon sequestration in the peridotite of the Samail Ophiolite, Sultanate of Oman. *Chemical Geology*, *330–331*, 86–100. https://doi.org/10.1016/j.chemgeo.2012.08.013

Peuble, S., Andreani, M., Godard, M., Gouze, P., Barou, F., Van De Moortele, B., et al. (2015). Carbonate mineralization in percolated olivine aggregates: Linking effects of crystallographic orientation and fluid flow. *American Mineralogist*, *100*(2–3), 474–482. https://doi.org/10.2138/am-2015-4913

Peuble, S., Godard, M., Luquot, L., Andreani, M., Martinez, I., & Gouze, P. (2015). CO2 geological storage in olivine rich basaltic aquifers: New insights from reactive-percolation experiments. *Applied Geochemistry*, *52*, 174–190. https://doi.org/10.1016/j.apgeochem.2014.11.024

Picazo, S., Malvoisin, B., Baumgartner, L. P., & Bouvier, A. S. (2020). Low temperature serpentinite replacement by carbonates during seawater influx in the Newfoundland margin. *Minerals*, *10*(2). https://doi.org/10.3390/min10020184

Pokrovsky, O. S., & Schott, J. (2002). Surface chemistry and dissolution kinetics of divalent metal carbonates. *Environmental Science and Technology*, *36*(3), 426–432. https://doi.org/10.1021/es010925u

Proskurowski, G., Lilley, M. D., & Brown, T. A. (2004). Isotopic evidence of magmatism and seawater bicarbonate removal at the endeavour hydrothermal system. *Earth and Planetary Science Letters*, *225*(1–2), 53–61. https://doi.org/10.1016/j.epsl.2004.06.007

Proskurowski, G., Lilley, M. D., Kelley, D. S., & Olson, E. J. (2006). Low temperature volatile production at the Lost City Hydrothermal Field, evidence from a hydrogen stable isotope geothermometer. *Chemical Geology*, *229*(4), 331–343. https://doi.org/10.1016/j.chemgeo.2005.11.005

Proskurowski, G., Lilley, M. D., Seewald, J. S., Früh-Green, G. L., Olson, E. J., Lupton, J. E., et al. (2008). Abiogenic Hydrocarbon Production at Lost City Hydrothermal Field. *Science*, *319*(5863), 604–607. https://doi.org/10.1126/science.1151194

Robinson, P. T., Malpas, J., Zhou, M. F., Ash, C., Yang, J. S., & Bai, W. J. (2005). Geochemistry and Origin of Listwanites in the Sartohay and Luobusa Ophiolites, China. *International Geology Review*, *47*(2), 177–202. https://doi.org/10.2747/0020-6814.47.2.177

1144 Rouméjon, S., & Cannat, M. (2014). Serpentinization of mantle-derived peridotites at mid-ocean
1145 ridges: Mesh texture development in the context of tectonic exhumation. *Geochemistry,*
1146 *Geophysics, Geosystems*, *15*(6), 2354–2379. https://doi.org/10.1002/2013GC005148

1147 Rouméjon, S., Früh-Green, G. L., Orcutt, B. N., & IODP Expedition 357 Science Party. (2018).
1148 Alteration heterogeneities in peridotites exhumed on the southern wall of the Atlantis
1149 Massif (IODP Expedition 357). *Journal of Petrology*, *59*(7), 1329–1358.
1150 https://doi.org/10.1093/petrology/egy065

1151 Rouméjon, S., Williams, M. J., & Früh-Green, G. L. (2018). In-situ oxygen isotope analyses in
1152 serpentine minerals: Constraints on serpentinization during tectonic exhumation at slow-
1153 and ultraslow-spreading ridges. *Lithos*, *323*, 156–173.
1154 https://doi.org/10.1016/j.lithos.2018.09.021

1155 Schandl, E. S., & Naldrett, A. J. (1992). CO2 metasomatism of serpentinites, south of Timmins,
1156 Ontario. *Canadian Mineralogist*, *30*, 93–108. Retrieved from
1157 http://citeseerx.ist.psu.edu/viewdoc/download?doi=10.1.1.558.3377&rep=rep1&type=pdf

1158 Schandl, E. S., & Wicks, F. J. (1991). Two stages of CO2 metasomatism at the Munro mine,
1159 Munro Township, Ontario: evidence from fluid-inclusion, stable-isotope, and
1160 mineralogical studies. *Canadian Journal of Earth Sciences*, *28*(5), 721–728.
1161 https://doi.org/10.1139/e91-062

1162 Schott, J., Pokrovsky, O. S., & Oelkers, E. H. (2009). The link between mineral
1163 dissolution/precipitation kinetics and solution chemistry. *Reviews in Mineralogy and*
1164 *Geochemistry*, *70*, 207–258. https://doi.org/10.2138/rmg.2009.70.6

1165 Schroeder, T. J., & John, B. E. (2004). Strain localization on an oceanic detachment fault system,
1166 Atlantis Massif, 30°N, Mid-Atlantic Ridge. *Geochemistry, Geophysics, Geosystems*,
1167 *5*(11). https://doi.org/10.1029/2004GC000728

1168 Schroeder, T. J., John, B. E., & Frost, R. B. (2002). Geologic implications of seawater
1169 circulation through peridotite exposed at slow-spreading mid-ocean ridges. *Geology*,
1170 *30*(4), 367–370.

1171 Schroeder, T. J., Bach, W., Jöns, N., Jöns, S., Monien, P., & Klügel, A. (2015). Fluid circulation
1172 and carbonate vein precipitation in the footwall of an oceanic core complex, Ocean
1173 Drilling Program Site 175, Mid-Atlantic Ridge. *Geochemistry, Geophysics, Geosystems*,
1174 *16*(10), 3716–3732. https://doi.org/10.1002/2015GC006041

1175 Schwarzenbach, E. M., Früh-Green, G. L., Bernasconi, S. M., Alt, J. C., & Plas, A. (2013).
1176 Serpentinization and carbon sequestration: A study of two ancient peridotite-hosted
1177 hydrothermal systems. *Chemical Geology*, *351*, 115–133.
1178 https://doi.org/10.1016/j.chemgeo.2013.05.016

1179 Schwarzenbach, E. M., Lang, S. Q., Früh-Green, G. L., Lilley, M. D., Bernasconi, S. M., &
1180 Méhay, S. (2013). Sources and cycling of carbon in continental, serpentinite-hosted
1181 alkaline springs in the Voltri Massif, Italy. *Lithos*, *177*, 226–244.
1182 https://doi.org/10.1016/j.lithos.2013.07.009

1183 Schwarzenbach, E. M., Gill, B. C., Gazel, E., & Madrigal, P. (2016). Sulfur and carbon
1184 geochemistry of the Santa Elena peridotites: Comparing oceanic and continental

processes during peridotite alteration. *Lithos*, *252–253*, 92–108. https://doi.org/10.1016/j.lithos.2016.02.017

Seifritz, W. (1990). CO2 disposal by means of silicates. *Nature*, *345*(June), 1990.

Seyfried, W. E., Pester, N. J., Tutolo, B. M., & Ding, K. (2015). The Lost City hydrothermal system: Constraints imposed by vent fluid chemistry and reaction path models on subseafloor heat and mass transfer processes. *Geochimica et Cosmochimica Acta*, *163*, 59–79. https://doi.org/10.1016/j.gca.2015.04.040

Spandler, C., Hermann, J., Faure, K., Mavrogenes, J. A., & Arculus, R. J. (2008). The importance of talc and chlorite "hybrid" rocks for volatile recycling through subduction zones; evidence from the high-pressure subduction mélange of New Caledonia. *Contributions to Mineralogy and Petrology*, *155*(2), 181–198. https://doi.org/10.1007/s00410-007-0236-2

Trommsdorff, V., & Evans, B. W. (1977). Antigorite-ophicarbonates: Phase relations in a portion of the system CaO-MgO-SiO2-H2O-CO2. *Contributions to Mineralogy and Petrology*, *60*(1), 39–56. https://doi.org/10.1007/BF00372850

Ulrich, M., Muñoz, M., Guillot, S., Cathelineau, M., Picard, C., Quesnel, B., et al. (2014). Dissolution-precipitation processes governing the carbonation and silicification of the serpentinite sole of the New Caledonia ophiolite. *Contributions to Mineralogy and Petrology*, *167*(1), 1–19. https://doi.org/10.1007/s00410-013-0952-8

Wetzel, L. R., & Shock, E. L. (2000). Distinguishing ultramafic-from basalt-hosted submarine hydrothermal systems by comparing calculated vent fluid compositions. *Journal of Geophysical Research: Solid Earth*, *105*(B4), 8319–8340. https://doi.org/10.1029/1999jb900382

Wheat, C. G., & Mottl, M. J. (2004). Geochemical fluxes through mid-ocean ridge flanks. *In Hydrogeology of the Oceanic Lithosphere*, 627–658.